Optimized shock-protecting microstructures

ZIZHOU HUANG, New York University, United States
DANIELE PANOZZO, New York University, United States
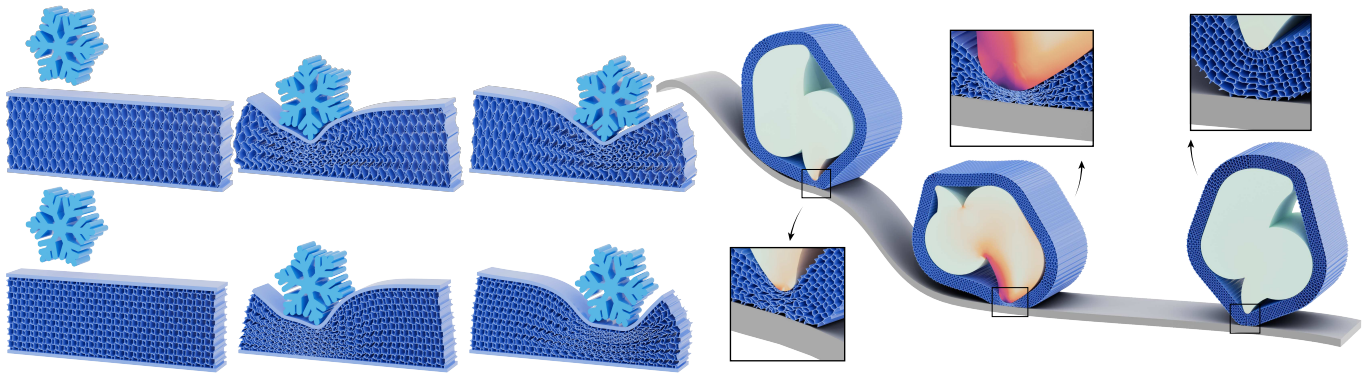DENIS ZORIN, New York University, United States

Fig. 1. Our shock-protecting microstructures are designed to provide a reaction force as close as possible to constant for a wide range of displacements. We introduce a computational pipeline to design a microstructure family, and we validate its effectiveness in simulations and in physical experiments. Our microstructures are able to protect irregular objects (left) and be used for package wrapping (right), simulated in 2D.

Mechanical shock is a common occurrence in various settings, there are two different scenarios for shock protection: catastrophic protection (e.g. car collisions and falls) and routine protection (e.g. shoe soles and mattresses). The former protects against one-time events, the latter against periodic shocks and loads. Common shock absorbers based on plasticity and fracturing materials are suitable for the former, while our focus is on the latter, where elastic structures are useful. Further, we optimize the effective elastic material properties which control the critical shock parameter, maximal stress, with energy dissipation by viscous forces assumed adequate. Improved elastic materials protecting against shock can be used in applications such as automotive suspension, furniture like sofas and mattresses, landing gear systems, etc. Materials offering optimal protection against shock have a highly non-linear elastic response: their reaction force needs to be as close as possible to constant with respect to deformation.

In this paper, we use shape optimization and topology search to design 2D families of microstructures approximating the ideal behavior across a range of deformations, leading to superior shock protection. We present an algorithmic pipeline for the optimal design of such families combining differentiable nonlinear homogenization with self-contact and an optimization algorithm. We validate the effectiveness of our advanced 2D designs by extruding and fabricating them with 3D printing technologies and performing material and drop testing.

Authors' addresses: Zizhou Huang, New York University, United States, zizhou@nyu.edu; Daniele Panozzo, New York University, United States, panozzo@nyu.edu; Denis Zorin, New York University, United States, dzorin@cs.nyu.edu.

1 INTRODUCTION

Mechanical shock is an abrupt and large increase in the surface force acting on an object, typically due to contact with an obstacle or another object. The need for protection from periodic mechanical shocks is common. For example, coil springs and leaf springs are extensively used in vehicle suspensions to provide a smoother ride and absorb vibrations from the road, springs are used in robotics to act as shock absorbers, allowing robots to move more smoothly while reducing wear and tear on mechanical components, and in medical devices like prosthetics and orthotics to absorb shocks during movement. In our body, cartilage is a natural shock absorber essential for our movement. In these cases, the shock happens periodically, and the acting forces have a known limited set of directions and magnitudes: the material must withstand multiple shocks, and it is thus common to use materials in their elastic deformation regime for these purposes. A plastic material would be unsuitable for these purposes, as it will have to be replaced after every shock.

A simple model problem, representative of most practical settings, is dropping a load with a layer of protective material on a rigid surface. The protective material layer performs two functions: first, it makes the deceleration of the object more uniform, reducing the maximal force acting on the load, and second, it converts the kinetic energy into elastic energy, partially dissipating it in the process. The latter most commonly happens due to the damping/visco-elastic properties of the protective material. The former function is critical,

as it eliminates the shock; the latter is desirable, as it eliminates oscillations and prevents bounces after the initial contact.

Minimization of maximal force/acceleration acting on the load requires materials with unusual properties: the optimal behavior is for the reaction force to remain constant as the protective material deforms (Section 3.1), which is very different from most common materials where the reaction force increases with deformation, for example in a spring. Materials with complex geometric structures such as foams or corrugated cardboard are commonly used as protective materials because their behavior is *essentially nonlinear*[1] and closer to the ideal behavior of having a constant decceleration.

In this paper, we describe how *shape optimization* for periodic microstructures consisting of 2D repeating cells can produce families of cell geometries with elastic response close to ideal over a large range of deformations, using a single base material. With our approach, we discover and present a family of optimized structures with ideal behavior up to 75% compression, leading to shock-absorbing materials significantly closer to the perfect fixed-force deceleration.

Our solution builds upon shape optimization algorithms for periodic metamaterials (e.g. methods producing families of cell structures spanning a particular range of effective material properties), extending them to support the distinctive features of shock-absorbing materials:

- The target constitutive law is *essentially nonlinear* and is not approximated well by a standard model, the homogenization must be performed in the nonlinear regime, sampling the whole stress-strain curve, rather than using a low-parametric model (e.g., captured by an elasticity tensor);
- *Self-contact* significantly impacts the structure behavior. The deformations are large, and contact must thus be considered in the shape optimization process;
- Large deformations require a *non-linear elasticity* model, and an accurate constitutive law for the base material must be used.
- *Tile symmetry*, which is a common feature of existing metamaterial families, is detrimental to shock absorption as it leads to unstable branching during the deformation.

The paper shows a complete algorithmic pipeline to construct nonlinear microstructure families parametrized by the target constant stress and how to use them to realize shock-absorbing materials. The contributions of our paper include the following:

- A novel family of single material shock-absorbing microstructures providing flat response curves to up to 75% compression (the previous known structure [Joodaky 2020] has a flat response up to 57%). The family is of independent interest from our algorithmic contribution and can be used directly to design and 3D print shock absorbers.
- We formulate the equations for computing effective elastic stress-strain dependence (homogenization) of nonlinear periodic structures with cells for large displacements in the presence of contact and non-linear base material constitutive law.

- We use a combinatorial enumeration of 2D structures to identify the best choices of structure topology for different regimes and obtain several families of cell structures with the best performance for different loads.
- We develop a gradient-based algorithm for shape optimization to minimize the deviation of the effective stress-strain dependence from the ideal constant-force behavior.
- We study the effect of tile symmetry and demonstrate that it must be avoided in the presence of large deformation.
- We validate the desired behavior of the resulting lattices by extensive experimental testing of fabricated lattice samples.

2 RELATED WORK

Microstructure design and optimization. There is an extensive literature on microstructure design, see, e.g., the survey [Kadic et al. 2019] for extensive references.

A lot of work on the optimization of geometry in individual cells is based on general shape and topology optimization methods [Allaire 2002; Bendsøe 1989; Bendsøe and Sigmund 2003]. Most of these works are based on small-displacement and linear material assumptions that are fundamentally not applicable in our setting. There is an increasing number of works considering nonlinear homogenization, which we review below.

In computer graphics, families of microstructures of various types were developed starting with [Panetta et al. 2015a; Schumacher et al. 2015; Zhu et al. 2017] with many more in studies in material science and engineering. We use the approach of [Panetta et al. 2015a] for our topology enumeration. Our nonlinear homogenization approach is similar to [Chen et al. 2021], based on [Nakshatrala et al. 2013].

Recently, [Li et al. 2022] used topology optimization to design microstructures to fit desired nonlinear stress-strain responses. They were also able to optimize microstructures to have a flat response. However, due to the limitation in topology optimization (Figure 23) and absence of contact, they only consider moderate compression of no more than 40% and a limited range of homogenized force (10N to 30N).

[Zhang et al. 2023] introduces a shape-optimization method to design microstructures modeled with a nearly isotropic response at finite strains. Collision avoidance is added to the objective function leading to structures that do not intersect up to a compression of 10%. The penalty does not handle contact, which unavoidably happens for higher compression rates, making it unsuitable for designing shock-absorbing materials.

A related and concurrent work [Li et al. 2023a] uses a neural network to map structure parameters to differentiable strain energy density, which is then used for inverse design. The model is trained on simulations that use a nonlinear material model and accurate contact modeling using the incremental potential contact model [Li et al. 2020]. The approach relies on sampling densely the parameter space and it is thus limited to a small number of parameters to model the geometry (2 for most of their microstructure families, with the larger family using 4). Instead of relying on a neural surrogate, we use a differentiable simulator to optimize the shape of the microstructures using parameterizations with up to 80 parameters. In addition to periodic simulations as in [Li et al. 2023a], we

---

[1]This term is commonly used in the materials literature to indicate that a non-linear material model is essential to capture the material's qualitative behavior.

perform full-simulation validation (in some cases, global effects are significant) as well as physical validation.

Shock-absorbing metamaterials. While the shock-absorbing properties of foams and structured materials were known for a long time, the desirable properties of certain types of lattices became known relatively recently. [Bunyan and Tawfick 2019] describes the χ-shaped cells, which have flattened regions in their stress-strain curves. This type of structure was further explored in [Joodaky 2020], which we consider as a baseline. [Chen et al. 2020] describes a shell-lattice metamaterial that can absorb very large energies while retaining a low density but does not attempt to optimize it.

Early work on designing shock-absorbing structured materials [Kellas and Jackson 2010] investigated designs of deployable honeycomb structures for crash energy management in light aircraft, showing these are superior to airbags. [Leelavanichkul et al. 2010] considered properties of a structure consisting of a helicoidal shell enveloping a cylinder, motivated by hydraulic shock absorbers. [Chen et al. 2018] describes a new hierarchical cellular structure created by replacing cell walls in regular honeycombs with triangular lattice configurations to improve energy absorption under uniaxial compression and shape integrity at high strains. [Matlack et al. 2016] described elastic metastructures with wide, low-frequency band gaps while reducing global mass, with applications in controlling structural vibrations, noise, and shock mitigation. These structures, however, are not close to the ideal shock-protecting structures we describe below.

[Mueller et al. 2019] analyzed the energy absorption properties of various periodic metamaterials, comparing them to foam-like random structures; while random structures exhibit better uniformity of stress for varying strain, periodic lattice geometries outperform their stochastic equivalents in terms of energy absorption in some cases. We show that periodic structures can be optimized to have high-stress uniformity. More recently, [Acanfora et al. 2022] explores maximizing energy absorption in shock absorbers while minimizing thickness or mass to improve transportation safety. Their analysis is restricted to six a priori chosen structures.

[Gongora et al. 2022] used a data-driven approach to infer the acceleration in the impact test from the stress-strain curve. The expensive transient simulation can be avoided with their approach while sacrificing some accuracy. However, they do not perform shape optimizations to find the optimal structures for impact protection.

[Huang et al. 2024] presents a general-purpose differentiable elastodynamics solver, but does not specifically address the problem of nonlinear inverse homogenization. This work demonstrates in Figure 13 an example of optimizing a structure composed of elements similar to Figure 31 using the shape representation from [Panetta et al. 2015a]. However, unlike other methods, they perform shape optimization in transient drop test simulations directly to minimize the L^4-norm of the stress on the load, directly on the complete structure without homogenization. Although this idea is straightforward, it suffers from several issues: (1) The stress distribution in transient simulations is very unstable and noisy both in space and in time (Figure 19), leading to less meaningful shape gradients and nonsmooth energy landscapes. (2) Transient full simulations are

much more expensive than periodic simulations, due to their large number of degrees of freedom and small time step size, especially when contact is considered. As a reference, compression of the 6×6 full microstructure in Figure 29 takes 75 min while the periodic 2×2 tile simulation takes 3 min. (3) The effectiveness of the optimized structure is restricted to that specific scene. It is hard to generalize to different load magnitudes as in our coverage (Figure 12) or different base materials without losing efficiency (Figure 30).

While some works do one or two parameter sweeps to identify best-performing structures, we are not aware of any works that performed structure optimization for shock absorption systematically.

We also briefly mention several papers that use bistable structures for shock absorption. In this case, the transition from one stable mode to a second stable mode allows the structure to store energy and yet be reversible, assuming no plastic deformation, as pointed out in [Frenzel et al. 2016; Shan et al. 2015]. This type of structure is suitable for protection against one-time shock (e.g., a fall), but cannot protect from repeated shocks, as encountered in shipping and transportation. Some examples of works of this type include [Ha et al. 2018; Izard et al. 2017], which describe tetra-beam-plate cells with snap-through behavior for large deflections. [Cao et al. 2021] surveys a variety of bistable structures with a focus on applications to actuators, MEMS, and shock absorption. Most recently, [Jeon et al. 2022] describes a realization of a common tilted-beam bistable structure with liquid crystal elastomers (LCE), with viscoelastic behavior improving energy absorption, and [Fancher et al. 2023] proposes a biomimetic shock-absorbing mechanism inspired by the bi-stable elongation behavior of a protein.

Nonlinear homogenization. Nonlinear homogenization of periodic structures for large displacements/strains is a far more complex problem than linear homogenization. In this case, the effective dependence between stress and strain requires multiple simulations. Even more fundamentally, for given boundary conditions for a periodic cell, the solution may be non-unique, and the material behavior may not even be fully captured by a local constitutive law. Nevertheless, suitable approximations of effective stress-strain dependencies were obtained under certain assumptions (e.g., [DeBotton et al. 2006]). We consider a version of the problem, with the stress-strain response for only one direction being of interest, which is considerably simpler than the general problem. As we have mentioned above, our nonlinear homogenization approach is similar to [Chen et al. 2021], based on [Nakshatrala et al. 2013], and used for microstructure design using topology optimization in [Wang et al. 2014].

We note that more general techniques for nonlinear homogenization were developed, but remain quite expensive. E.g, [Yvonnet and He 2007] and [Schröder 2014] use reduced-order models for homogenization obtained using proper orthogonal decomposition (POD) to increase efficiency. These methods are further extended in [Fritzen and Kunc 2018], [Kunc and Fritzen 2019] and [Kunc and Fritzen 2020], with a typical approach of first constructing a reduced-order model, then sampling deformation space using this model, and finally interpolating the samples using various types of interpolation.
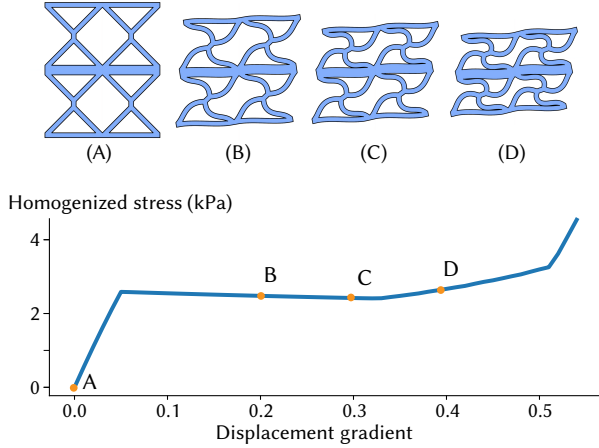
Fig. 2. Deformation and stress-strain curve of the microstructure proposed in [Joodaky 2020]. Contact may happen in the region where stress does not increase.

Several works use nonlinear, finite strain homogenization in the topology optimization context to obtain periodic metamaterials with desired properties, starting with [Wang et al. 2014], which uses numerical tests of response to a deformation, which can be considered partial homogenization, in the context of truss-based and continuum topology optimization. A more general case of homogenization is [Behrou et al. 2021]. [Wallin and Tortorelli 2020a] describes how non-linear homogenization based on the multiscale virtual power method can be used in the context of topology optimization, with sensitivities transferred from microscale to macroscale. While our method is somewhat related to topology optimization methods as we use an implicit shape representation described in [Panetta et al. 2017], unlike these techniques, it supports accurate differentiable contact.

[Xue and Mao 2022a] uses a formulation for cellular metamaterial optimization for large deformations based on the shape map, mapping a fixed reference configuration to an optimized one. Our method, while using an implicit shape representation, uses a similar discretization at each step to compute the shape derivatives.

In computer graphics literature, bistable auxetic structures are described in [Chen et al. 2021] and used for deployable surfaces; [Sperl et al. 2020] simulates yarn-level cloth effects using nonlinear homogenization; [Schumacher et al. 2018] proposes a comprehensive approach to characterizing the mechanical properties of structured sheet materials with nonlinear homogenization and uses inverse design to explore structures with desired properties.

[Zhang et al. 2023] proposes a collision penalty term to avoid intersections in the deformed microstructures. Although it avoids the expensive contact-aware simulation, it prevents any contact throughout the simulation. As in Figure 2, contact may happen in some optimal microstructures for shock protection, even in the strain range where the stress does not increase.

3 METHOD

3.1 Background and problem formulation

We start with reviewing the problem setup (Figure 3) for measuring the shock-protective properties of a material.

A (meta)material is typically characterized by the stress-strain curve $\sigma(\epsilon)$. Since a response to a one-dimensional load is of primary interest to us, in the model setup we only consider one diagonal component of the stress corresponding to vertical compression and its dependence on the applied strain along the same direction. I.e., we consider curve $\sigma = \sigma(\epsilon)$, where σ is a scalar stress, and ϵ is the scalar strain.

Ideal shock-protective material. Suppose the kinetic energy of an object is $mv^2/2$ right before impact, where m is the object mass, v is its velocity. Let A be the area of contact with the protective material. Ignoring gravity, the force acting on the object as the protective material is compressed to strain ϵ is $F = A\sigma(\epsilon)$. The assumption that the object stops for some $\epsilon < 1$, can be expressed as

$$Ah \int_0^1 \sigma(\epsilon)d\epsilon \geqslant mv^2/2,$$

where h is the protective layer thickness; i.e., that the work of the elastic force over this thickness is larger than the kinetic energy before contact. Here, we approximate the strain by modeling it as constant over the thickness of the layer. While in reality there may be considerable variation, this assumption is needed to obtain a problem formulation independent of the protective layer thickness/geometry.

This leads to the following optimization problem for the "ideal" stress-strain curve:

$$\min_\sigma \max_\epsilon \sigma(\epsilon), \text{ subject to } \int_0^1 \sigma(\epsilon)d\epsilon \geqslant \sigma_f,$$

where $\sigma_f = mv^2/(2Ah)$. It is easy to see that the optimal solution is $\sigma(\epsilon) = \sigma_f$, as if $\sigma \leqslant \sigma_f$ everywhere on $[0, 1]$, the constraint can only be satisfied if the equality holds, and if $\sigma > \sigma_f$ anywhere, this choice of $\sigma(\epsilon)$ is suboptimal, because the constant σ is valid and has a lower maximum.

Seemingly the ideal shock-protective material can only absorb 2× energy compared to a perfect linear elastic material with a linear stress response $\sigma(\epsilon) = C\epsilon$. However, it's actually hard to find materials with perfect linear response at finite strains, especially for large compression: The recent work [Zhang et al. 2023] manages to optimize microstructures to stay close to linear response up to 15% strain, while we consider compression up to 75%.

Optimization problem. Such a flat response is not physically possible: when $\epsilon = 1$ the reactive forces have to increase to infinity; similarly, close to $\epsilon = 0$, the reactive forces have to be close to zero. So for any real (meta)-material, there is a ramp-up part of the curve, a flat part, and a final part, corresponding to extreme compression. This leads to the following optimization problem:

For a base material and a target value of stress σ_f, optimize the geometry of a unit cell so that the stress-strain curve for a metamaterial obtained by periodically repeating it is as close as possible to $\sigma(\epsilon) = \sigma_f$.

Solving this problem yields a family of cell geometries parametrized by the effective stress σ_f. For each value of σ_f, we obtain a different

Fig. 3. Model problem setup.

Fig. 4. A cell topology T is annotated with geometric parameters r (a radius and a 2D position for each vertex). The inflator Ψ converts the graph representation into an implicit function, which is then triangulated to obtain a mesh representation $\bar{q}$ of the cell domain Ω.
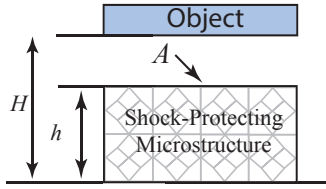
geometry and, thus, a different stress-strain curve with a large flat region. We note that the size of the flat region is not uniform within the family: our objective is to make it as large as possible for each effective stress value.

To the best of our knowledge, such a family of materials has never been studied before. As discussed in Section 2, examples of geometries for specific σ_f have been reported, but not a complete family covering a large range of stress values.

To illustrate how such a family of materials can be used, we consider the following standard problem: given maximal allowed deceleration G, and expected drop height H, choose the optimal material in the family and required thickness. Conservatively, assuming that all deceleration happens at the flat part of the response curve and approximating the strain by constant, we obtain σ_f from the force balance $mG = A\sigma_f$; note that this does not depend on the thickness of the protective layer, and allows us to pick a material already. For a specific material in the family corresponding to σ_f, we require that the work done by elastic forces on the flat part of the stress-strain curve is sufficient to absorb the kinetic energy, i.e. (approximately) $\alpha(\sigma_f)\sigma_f = \frac{mgH}{h}$ from which thickness h can be estimated.

3.2 Approach overview

We obtain the families of protective metamaterials using a combination of combinatorial enumeration of topologies and shape optimization. The main components of our algorithm include:

- **Topology enumeration and geometric parametrization (Section 3.3).** The topology of our cells is defined by a graph within the cell, with geometric parameters given by radii at graph nodes and blend parameters, as shown in Figure 4. The outer loop of the overall algorithm enumerates different possible topologies.
- **Nonlinear differentiable homogenization (Section 3.4).** The objective of our optimization is the deviation of the stress-strain curve $\sigma(\epsilon)$ from a constant σ_f. To obtain the effective stress $\sigma(\epsilon)$, we use periodic nonlinear homogenization with *contact*, obtaining effective stresses for a set of background deformations ϵ. Contact is of particular importance in our setting as the material is designed specifically for very large deformations. Along with computing effective stresses, we compute their gradients with respect to shape parameters, which are essential for efficient optimization.
- **Objective and optimization (Section 3.5).** For every topology and a target flat stress value σ_f, we optimize the shape
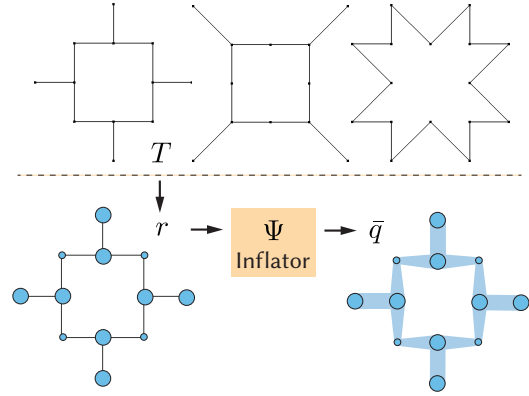
to minimize the deviation of effective stress from σ_f, computed via homogenization, for strains sampled at a fixed set of strains ϵ_i.

Nonlinear differentiable homogenization is the core part of the algorithm; we discuss it in detail after briefly reviewing topology enumeration, starting with the forward simulation and then explaining how the derivatives can be computed.

3.3 Topology enumeration and geometric parametrization

We use the graph representation introduced in [Panetta et al. 2015a] to represent our periodic cells and the implicit surface definition proposed in [Panetta et al. 2017], which we briefly review here.

Cell parametrization and graph inflator. Each microstructure is parametrized by a graph T, annotated with a radius and a position for every graph node (stacked in a single vector of parameters r), embedded in a rectangle of size $a \times b$. [Panetta et al. 2017] defines an implicit surface that "inflates" the graph based on the radii assigned to its vertices; a periodic triangular mesh of the domain Ω is then obtained from the implicit function using marching squares. The map from the parameters r and cell dimensions a, b to the vector of periodic vertex positions $\bar{q}$ is denoted

$$\bar{\mathbf{q}} = \Psi_T(r, a, b).$$

The derivatives of the vertex positions in this mesh with respect to shape parameters (i.e. the shape velocities) are computed using implicit function differentiation ([Panetta et al. 2017]).

Design space. The design space of the shape consists of three parts: combinatorial choice of the graph T, microstructure shape parameters r, and the size of unit cell a, b. We fix $b = 1$ since uniform scaling of the cell uniformly does not affect the homogenized properties. However, the ratio between the width and length of the cell affects the stress-strain curve as in Figure 5 (even for linear elasticity).

For the choice of topology, we consider 105 patterns in 2D following [Panetta et al. 2015b], generated by enumeration of patterns
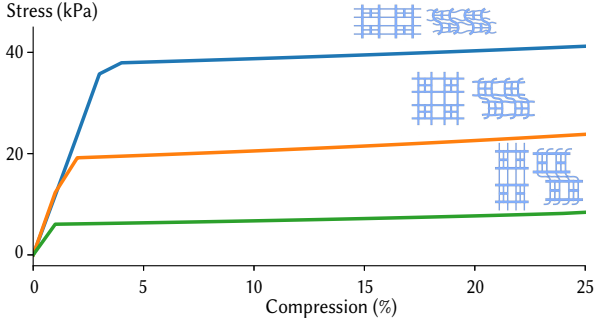
Fig. 5. Ratio between the width and length of the unit cell affects the stress-strain curve. Different curves are not simply the same up to a constant scaling factor due to nonlinearity.

with bounded number over vertices in the cell and number of edges meeting at a vertex. In the optimization, we first generate the mesh in the unit square based on the graph and its parameters. Then, we scale the shape by the scale parameters to get the unit cell in a rectangle.

3.4 Nonlinear homogenization

A periodic metamaterial consists of repeating cells with identical geometry $\bar{q} = \Psi(r, a, b)$, parametrized by the shape parameters r and cell dimensions. The effective (homogenized) properties of the material are obtained in the limit of cells repeated infinitely, and deformations are considered at a scale much larger than the cell size; in this case, we can assume that the metamaterial behaves as a homogeneous solid material, with an effective constitutive law, relating stress to strain at each point. This stress-strain dependence can be obtained from the constitutive law of the base material and cell geometry by *homogenization.*

While for our problem the dynamic behavior of the material may be important we consider *static* deformations only in our optimization, which captures the most significant aspects of the behavior of highly absorbing materials. We do not include dissipation in our simulation as it does not affect the effectiveness of protection (Figure 17). We also assume negligible plasticity which is a valid assumption for materials chosen to provide protection from repeated shock. The deformation of the metamaterial can be decomposed into a slow-changing deformation, that can be computed from the (a priori unknown) macroscopic constitutive law, and a cell-scale fluctuation. At a level of a single cell, macroscopic stress and strain can be viewed as constant, i.e., corresponding to a linear deformation of the cell, with a periodic cell fluctuation $\tilde{u}$ added on top. Homogenization assumes that there is a constant macroscopic strain, equivalently, a linear deformation Gx where x is the spatial coordinate (test deformation), solves for the periodic fluctuation $\tilde{u}$ and computes the resulting effective stress.

For small displacements, a linear effective constitutive law $\sigma = C\epsilon$ can be assumed, fully determined by components of an effective elasticity tensor, which considerably simplifies the problem: the elasticity tensor can be fully inferred from a small number of test

deformations. However, the materials we aim to construct are inherently nonlinear (Figure 29). In this case, to approximate the effective stress-strain dependence, we must compute the effective stress resulting from a larger set of finite deformations. The need for sampling for our problem is considerably reduced by considering only stress-strain dependence for a single direction.

Notation. We use x to denote the coordinate on the periodic cell $\Omega \subset V$, where V is a rectangular tiling with tiles of size $a \times b$. We use $u(x) = \tilde{u}(x) + Gx$ to denote the solution of the elasticity equations with contact, where $\tilde{u}$ is the periodic fluctuation part and Gx is the macroscopic linear deformation part, with $G \in \mathbb{R}^{2 \times 2}$. We restrict matrices G to be symmetric to eliminate rotational components of the deformation, which do not affect elastic behavior. The domain Ω is discretized into a periodic triangular mesh.

The vector of coefficients of $\tilde{u}(x)$ in a FE basis ϕ_i is denoted $\tilde{\mathbf{u}}$ (we use quadratic elements); this vector includes degrees of freedom only, i.e., the periodicity conditions on $\mathbf{u}$ are used to exclude values on the right and upper boundaries of V.

We denote the vertices of this mesh x_i, with the vector of vertices of size N denoted $\mathbf{x}$. These are determined by the shape parameters r as described above. We use piecewise-linear basis ξ_i to represent changes in the mesh as the shape parameters are varied. For the discrete solution $\mathbf{u}$, the following equation holds:

$$\mathbf{u} = \tilde{\mathbf{u}} + \mathbf{x}G^T, \tag{1}$$

where $\tilde{\mathbf{u}}$ is the discretization of the fluctuation. As explained below, the variables in the elasticity equations we solve to compute the homogenized stress-strain dependence are $\mathbf{u}$ and components G^{00}, G^{01} of the deformation matrix G. We denote the vector of all of these variables $\mathbf{v} = [\tilde{\mathbf{u}}; G^{00}, G^{01}]$.

Sampling effective stress. As our focus is on response to loads in a single direction, we sample a single diagonal component of the stress tensor corresponding to vertical deformation, and how it relates to the component of the macroscopic deformation G in the vertical direction. This yields a sampled approximation of a stress-strain curve. In other words, the result of our homogenization procedure is a set of samples $\sigma(\epsilon_i)$ approximating the dependence $\sigma(\epsilon)$.

For each sample value of $G^{11} = \epsilon$, we set up a nonlinear elasticity problem to determine corresponding stress. We assume that the material is free to deform in other directions; for this reason, we include the components G^{00} and G^{01} as variables in our optimization:

$$\min_{\tilde{\mathbf{u}}, G} W(\tilde{u}, G) \quad \text{such that } G^{11} = \epsilon, \tag{2}$$

where $W := W_e + W_c$ is the sum of elastic (Equation 4) and contact barrier energy (Equation 5 in [Li et al. 2023b]). The effective stress tensor corresponding to ϵ can be computed as

$$\bar{\sigma}(\epsilon) := \frac{1}{|V|} \int_\Omega \sigma(\nabla_x \tilde{u} + G) dx, \tag{3}$$

where $|V|$ is the area of V in 2D.

Elasticity. The elastic energy has the form

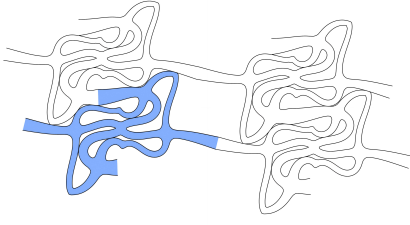$$W_e := \int_\Omega w_e(\nabla_x \tilde{u} + G) dx, \tag{4}$$

Fig. 6. A deformed periodic cell collides with its tiled boundary mesh during homogenization. Accounting for collision is crucial to designing a shock-protecting microstructure family (Figure 24).

(A)   (B)   (A)   (B)   (C)

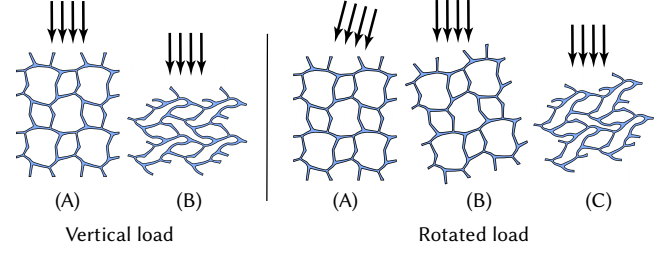Vertical load   Rotated load

Fig. 7. Homogenizations with both vertical and rotated loads. The rest shape (A) and its compression (B) under vertical load are shown on the left. For rotated loads on the right, instead of changing the force direction as in (A), we rotate the rest shape instead in (B). The compressed shape is shown in (C).

where $w_e : \mathbb{R}^{2 \times 2} \to \mathbb{R}$ is the Neo-Hookean energy density function

$$w_e(F - I) := \frac{\mu}{2}(\text{Tr}[FF^T] - 2 - 2\log(\det F)) + \frac{\lambda}{2}\log^2(\det F),$$

where F is the deformation gradient, λ and μ are the Lamé parameters. To solve (2) the Jacobian and Hessian of the elastic energy are needed to solve the elasticity equation. The gradient and Hessian of the elastic energy with respect to F are:

$$\sigma := \nabla w_e \in \mathbb{R}^{2 \times 2}, \quad C := \nabla^2 w_e \in \mathbb{R}^{2 \times 2 \times 2 \times 2}.$$

Then we have the following expressions for the components of the gradient and Hessian:

$$\partial_{\mathbf{u}_i} W_e = \int_\Omega \sigma(\nabla u) : \nabla \phi_i dx \quad \partial_{\mathbf{u}_i, \mathbf{u}_j} W_e = \int_\Omega \nabla \phi_i : C(\nabla u) : \nabla \phi_j dx,$$

where $i, j = 1, \ldots, N$. The first and second derivatives of W_e with respect to v are obtained by applying the chain rule of Equation 1.

Periodic contact. To adapt IPC [Li et al. 2020] to the periodic homogenization, we need to consider contact inside the periodic cell and between geometry from adjacent cells. We assume that we do not need to consider contact between geometry in cells that are not adjacent: although this may theoretically happen, we have not observed this even for extreme deformations. To handle contact, we use a 2×2 tiling of the deformed periodic cell in the collision detection and barrier energy computation. We observe that due to periodicity, it is sufficient to consider neighbors only below and to the left of a given cell, not above and to the right.

Figure 6 shows how the tiled boundary mesh of a deformed periodic cell is used to detect collisions between cells.

Define $\mathbf{u}^t$ as the vector of displacements on the 2×2 tile. In the two-by-two tiling of copies of the periodic domain V, the coordinates of vertices of three tiles are given by $\mathbf{x}_i + a\mathbf{e}_1$, $\mathbf{x}_i + b\mathbf{e}_2$, $\mathbf{x}_i + a\mathbf{e}_1 + b\mathbf{e}_2$, where $\mathbf{e}_d$ ($d = 1, 2$) is the unit vector along d-th axis. We concatenate these along with the original domain degrees of freedom into a vector $\mathbf{x}^t$ of size M. The index mapping I, maps vertex j on the tiled mesh to the corresponding vertex $I(j)$ on the original mesh. The displacement on the tiled mesh $\mathbf{u}^t \in \mathbb{R}^{M \times 2}$ can be represented as

$$\mathbf{u}_j^t = \tilde{\mathbf{u}}_{I(j)} + G\mathbf{x}_j^t, \tag{5}$$

where x_j^t is the position of vertex j on the tiled mesh. The Jacobian and Hessian of the barrier energy with respect to u^t are identical to

the ones used in [Li et al. 2020]. We apply the chain rule based on (5) to obtain the Jacobian and Hessian with respect to $\mathbf{v}$:

$$d_{\mathbf{v}} W_c = (d_{\mathbf{u}^t} W_c)(d_{\mathbf{v}} \mathbf{u}^t)$$
$$d_{\mathbf{v}}^2 W_c = (d_{\mathbf{v}} \mathbf{u}^t)^T (d_{\mathbf{u}^t}^2 W_c) d_{\mathbf{v}} \mathbf{u}^t,$$

where W_c is the contact barrier potential, $d_{\mathbf{v}} \mathbf{u}^t$ is the gradient of the linear mapping in Equation 5. Entries of $d_{\mathbf{v}} \mathbf{u}^t$ can be computed by

$$\partial_{\tilde{\mathbf{u}}_{id}} \mathbf{u}_{jk}^t = \delta_{dk}\delta_{I(j),i} \qquad i = 1, \ldots, N; \; j = 1, \ldots, M; \; d, k = 1, 2$$
$$\partial_{G_{dp}} \mathbf{u}_{jk}^t = \delta_{dk}\mathbf{x}_{jp}^t \qquad j = 1, \ldots, M; \; d, p, k = 1, 2$$

$$(6)$$

where δ_{ij} is the Kronecker delta.

Non-uniaxial Load. We also consider non-uniaxial loads in the nonlinear homogenization to protect shocks in different directions. Similar to the problem (2), instead of fixing G^{11}, one can fix the compression strain in the load direction, which becomes a linear equality constraint. To avoid enforcing such constraints, we rotate the shape instead so that the resulting load is still in the Y direction (Figure 7). In this way, we do not need to change the formulation of the homogenization but only need to consider the influence of the rotation in the shape derivatives. In our experiments, we study perturbations around the Y direction between $-15°$ to $15°$.

Tile Symmetry. We note that we do not enforce rotation and reflectional symmetry on the cell geometry during optimization. This is in contrast with most two-scale microstructure design works (such as [Li et al. 2022; Zhang et al. 2023]), which use symmetry as a natural way to reduce the parameter space.

As we show in Figure 28, symmetric tiles are problematic for large strains (over 10 % compression), as they can buckle symmetrically, leading to different deformed geometries in each tile, which can lead to large differences between the homogenized result and the full-scale simulation of a tiling.

We experimentally discovered that removing the symmetry constraints is sufficient to obtain asymmetric deformations consistent with the homogenized results, which do not suffer from this issue.
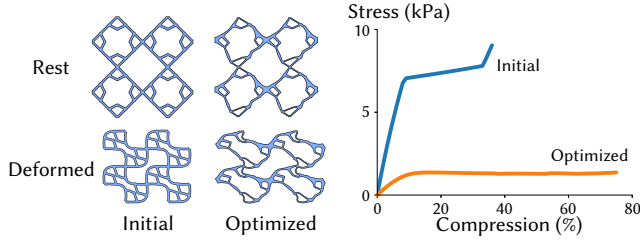
Fig. 8. Each microstructure topology is initialized with a default set of positions and radii for each vertex. Before optimization (left) the stress (Pa) - strain curve is far from flat; after optimization (right) the curve is flat over a large range of deformation.

3.5 Objective and optimization algorithm

Objective. Given a target scalar stress $\sigma_f > 0$, the goal of the optimization is to minimize the deviation of the effective stress from σ_f on the compression strain range of $[10\%, \epsilon]$, where $\epsilon < 1$ is the max compression strain we consider. We initialize $\epsilon = 25\%$ in the first optimization and gradually increase it in the following optimizations until it cannot be reached.

In every optimization, the forward simulation is solved on a series of scalar compression strains ϵ_i ($i = 0, 1, \dots$) uniformly sampled in the interval $[10\%, \epsilon]$ (with stride 5%), the corresponding homogenized stress and macro strain are $\bar{\sigma}_i$ and G_i, the objective is

$$J(\mathbf{q}) := \sum_i (\frac{\bar{\sigma}_i(1,1)}{\sigma^*} - 1)^2 + w(|G_i^{01}|^2 + |G_i^{00}|^2), \quad (7)$$

where σ^* is the target homogenized stress, and $\mathbf{q} = (r, a, b)$ are the shape parameters and the size of the cell. The second term penalizes shear and horizontal deformation under compression (essentially forcing the Poisson's ratio to be nearly 0), we pick $w = 50$ in the optimizations. We refer to Section 4.8 for a discussion on why shear or horizontal deformations are highly undesirable in our setting. Figure 8 shows an example of how the stress-strain curve changes after the optimization and how the geometry of the microstructure tile changes.

Algorithm. We provide the pseudocode of our complete optimization and simulation algorithms in Appendix B, and we will release a reference open-source implementation of our algorithm.

In rare cases, Newton's method converges to a saddle point instead of a local minimum. Saddle points of the elastic energy are normally physically undesired since they are unstable in reality and may switch to a local minimum under small perturbations. In this case, we drop the saddle point solution and rerun the simulation with a small initial perturbation. Note that as discussed in Appendix B, it rarely falls into a saddle point with our proposed method.

Incremental load. We use the incremental load method [Ogden 1992] for forward simulations. However, enforcing high compression strain on an arbitrary structure may result in high contact forces, causing convergence issues in IPC, so we optimize every structure incrementally: We first optimize the shape so that its homogenized stress reaches the target in the strain range $[10\%, 25\%]$,

then increase the max strain by 5% at a time and use the previously optimized shape as the initial guess.

As shown in Figure 9, the deformation of some microstructures cannot be fully captured by simulations on a single periodic cell since the deformation in the microstructure is not periodic in terms of every single cell. This behavior also happens in other microstructures as studied in [Bertoldi et al. 2010; Xue and Mao 2022b]. To avoid the inconsistency caused by this behavior, we perform optimizations using the homogenization on 2×2 tiles.
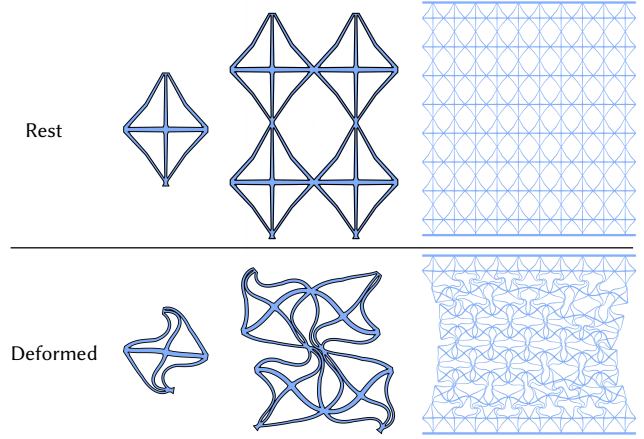

Fig. 9. Homogenization on a single cell fails to capture the behavior in full simulations. From left to right: homogenization on a single cell, homogenization on a 2×2 tile, full simulation without periodicity.

Figure 10 shows three examples of how the objective and its gradient reduce in the shape optimization. Since our goal is to reduce the objective until the homogenized stress is close enough to the target, for better efficiency, we stop the optimization when the pointwise error is smaller than the threshold (5%), even if the gradient is not small enough. Still, the gradient norm reduces by over 3 orders of magnitude in the optimization, which is plenty considering the difficult contact simulations.

Warm start. When optimizing the shapes of the same topology for different homogenized stresses (Figure 12), one can use the optimized shape with homogenized stress σ_1 to generate the initial guess shape for the optimization towards homogenized stress σ_2. However, notice that in Figure 5, the aspect ratio of the unit cell changes the scale of the stress curve and does not change the overall behavior much. Inspired by this, once the optimized shape at σ_1 is obtained, we first minimize Equation 7 by only optimizing the aspect ratio b/a, then perform the full shape optimization to further minimize the objective. Note that the dependence of $\bar{\sigma}$ on b/a is not linear, e.g. in Figure 5 the curve of $b/a = 2$ is around $2\times$ of $b/a = 1$ and $6\times$ of $b/a = 0.5$.

3.6 Shape derivatives

We optimize Objective (7) of Section 3.5 (OBJECTIVE($\mathbf{q}, \tilde{\mathbf{u}}, G$) in the pseudocode) with respect to the microstructure cell parameters $\mathbf{q} = (r, a, b)$. We will overload the notation (whenever the derivation
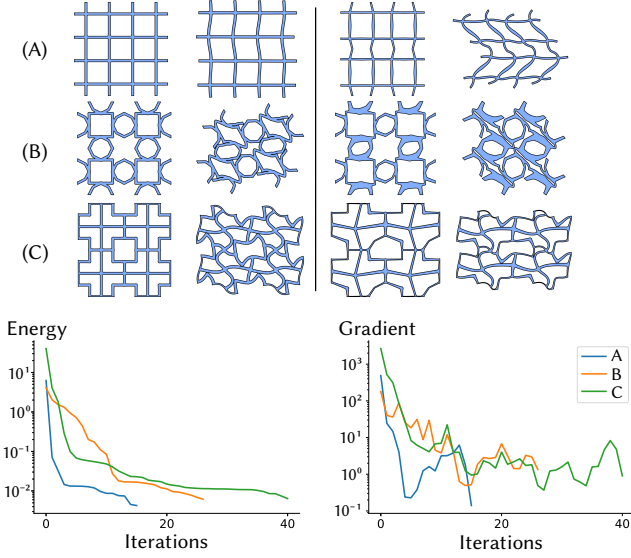
Fig. 10. The objective and gradient plots for the shape optimizations (bottom). On the top from left to right: Initial rest shape, initial deformed shape, optimized rest shape, optimized deformed shape.

is generic) and use $\mathbf{q}$ to refer to the independent vertex positions $\bar{\mathbf{q}} = \Psi(r)$ defining domain Ω (we eliminate a subset of boundary vertices due to periodicity) or to the cell dimensions $\tilde{\mathbf{q}} = (a, b)$.

As the cell scale is typically determined by fabrication constraints we can use box constraints to keep one of the scale dimensions close to the desired size. Shape parameters (graph vertex positions and radii) determine vertex positions, as described in Section 3.3.

The derivatives of the objective J with respect to the shape parameters are computed using the adjoint method, with which the shape derivatives can be obtained by solving a single additional linear equation, and then evaluating an expression depending on this unknown. See Appendix A for the derivation of the adjoint method. Due to the periodic boundary condition, extra variable G in the simulations, and the periodic contact, [Huang et al. 2024] cannot be applied trivially to our case. We summarize the extra adjoint terms below.

Shape derivative of elastic force $\partial_{\mathbf{q}} \partial_{\mathbf{v}} W_e$. Since the elastic energy is in the form of an integral over the domain:

$$W_e = \int_\Omega w_e(\nabla \tilde{u} + G)dx,$$

we can first compute the shape derivatives with respect to all vertices in $\mathbf{x}$, then apply the chain rule of $\mathbf{q} \rightarrow \mathbf{x}$,

$$\partial_{\mathbf{x}} \partial_{\mathbf{v}} W_e = \partial_{\mathbf{x}}(\partial_{\mathbf{u}} W_e \partial_{\mathbf{v}} \mathbf{u})$$
$$= (\partial_{\mathbf{x}} \partial_{\mathbf{u}} W_e) \partial_{\mathbf{v}} \mathbf{u} + \partial_{\mathbf{u}} W_e (\partial_{\mathbf{x}} \partial_{\mathbf{v}} \mathbf{u}),$$

where $\partial_{\mathbf{x}} \partial_{\mathbf{v}} \mathbf{u}$ can be obtained by differentiating Equation 1, and for $\partial_{\mathbf{x}} \partial_{\mathbf{u}} W_e$ we follow the derivation in [Huang et al. 2024], here we only write down the final formula. Recall that ξ_i is the linear basis

used to represent the change of the rest mesh, then

$$\partial_{\mathbf{x}_i} \partial_{u_j} W_e = \partial_{\mathbf{x}_i} \int_\Omega \sigma : \nabla \phi_j dx$$
$$= \int_\Omega -\sigma \nabla \xi_i^T : \nabla \phi_j - \nabla \phi_j : C : \nabla u \nabla \xi_i + (\sigma : \nabla \phi_j) \nabla \cdot \xi_i.$$

Shape derivative of contact force $\partial_{\mathbf{q}} \partial_{\mathbf{v}} W_c$. The periodic contact force can be considered as a function of vertices of the tiled mesh, we follow [Huang et al. 2024] to compute the derivatives of the contact force with respect to vertex positions on the tiled mesh, then apply the chain rule to the map $\mathbf{q} \rightarrow \mathbf{x}^t$, which we discuss below.

For every vertex j on the tiled mesh, its position can be written as

$$\mathbf{x}_j^t = \bar{\mathbf{q}}_{I(j)} + \tilde{\mathbf{q}}^T \begin{pmatrix} \alpha_j & 0 \\ 0 & \beta_j \end{pmatrix} \quad \text{for some } \alpha_j, \beta_j \in \{0, 1\}, \quad (8)$$

where (α_j, β_j) are indices of the tile to which the vertex belongs, i.e., shifts by a or b the components of the scale part of $\mathbf{q}$. To recall, $I(j)$ maps the index of vertices on the tiled mesh back to the index of vertices on the single-cell mesh. Then

$$\partial_{\bar{\mathbf{q}}_i} \partial_{\mathbf{v}} W_c = \partial_{\bar{\mathbf{q}}_i}(\partial_{\mathbf{u}^t} W_c \partial_{\mathbf{v}} \mathbf{u}^t)$$
$$= \partial_{\mathbf{u}^t} W_c \partial_{\bar{\mathbf{q}}_i} \partial_{\mathbf{v}} \mathbf{u}^t + \partial_{\bar{\mathbf{q}}_i} \partial_{\mathbf{u}^t} W_c \partial_{\mathbf{v}} \mathbf{u}^t$$
$$= \partial_{\mathbf{u}^t} W_c \partial_{\bar{\mathbf{q}}_i} \partial_{\mathbf{v}} \mathbf{u}^t + (\sum_{I(j)=i} \partial_{x_j^t} \partial_{\mathbf{u}^t} W_c) \partial_{\mathbf{v}} \mathbf{u}^t$$

$$\partial_{\tilde{\mathbf{q}}} \partial_{\mathbf{v}} W_c = \partial_{\tilde{\mathbf{q}}}(\partial_{\mathbf{u}^t} W_c \partial_{\mathbf{v}} \mathbf{u}^t)$$
$$= \partial_{\mathbf{u}^t} W_c \partial_{\tilde{\mathbf{q}}} \partial_{\mathbf{v}} \mathbf{u}^t + \partial_{\tilde{\mathbf{q}}} \partial_{\mathbf{u}^t} W_c \partial_{\mathbf{v}} \mathbf{u}^t$$
$$= \partial_{\mathbf{u}^t} W_c \partial_{\tilde{\mathbf{q}}} \partial_{\mathbf{v}} \mathbf{u}^t + (\sum_j \begin{pmatrix} \alpha_j & 0 \\ 0 & \beta_j \end{pmatrix} \partial_{\mathbf{x}_j^t} \partial_{\mathbf{v}} W_c) \partial_{\mathbf{v}} \mathbf{u}^t.$$

The gradient with respect to $\mathbf{q}$ can then be obtained by applying the chain rule to the map $\mathbf{q} \rightarrow [\bar{\mathbf{q}}, \tilde{\mathbf{q}}]$. In the above equations, the terms we have not discussed yet are $\partial_{\bar{\mathbf{q}}_i} \partial_{\mathbf{v}} \mathbf{u}^t$ and $\partial_{\tilde{\mathbf{q}}} \partial_{\mathbf{v}} \mathbf{u}^t$, which can be computed by combining Equations (6) and (8).

Derivatives of effective stress $\partial_{\mathbf{q}} J, \partial_{\mathbf{v}} J$. To compute derivatives of Equation 7 with respect to $\mathbf{q}$ and $\mathbf{v}$, the only difficulty is in

$$\bar{\sigma}^{11} = \frac{1}{|V|} \int_\Omega \sigma^{11}(\nabla \tilde{u} + G)dx.$$

Similar to the elastic force, it is also in the form of an integral of the stress tensor over the unit cell domain, except that the gradient of the basis function is replaced by identity, so one can derive derivatives following the derivation for elastic forces.

4 EVALUATION

We implemented our algorithm in C++ and used Eigen [Guennebaud et al. 2010] for the linear algebra routines, a modified version of PolyFEM [Schneider et al. 2019] for finite element simulation, triangle [Shewchuk 2005] for meshing, and Pardiso [Alappat et al. 2020; Bollhöfer et al. 2019, 2020] for solving linear systems. All our experiments are run on cluster nodes with an Intel Cascade Lake Platinum 8268 processor limited to 16 threads.

We first show the coverage of our microstructure family in the space of (strain, stress) pairs: a point (σ_f, ϵ) is considered covered if for strain ϵ the actual response of the microstructure in the family
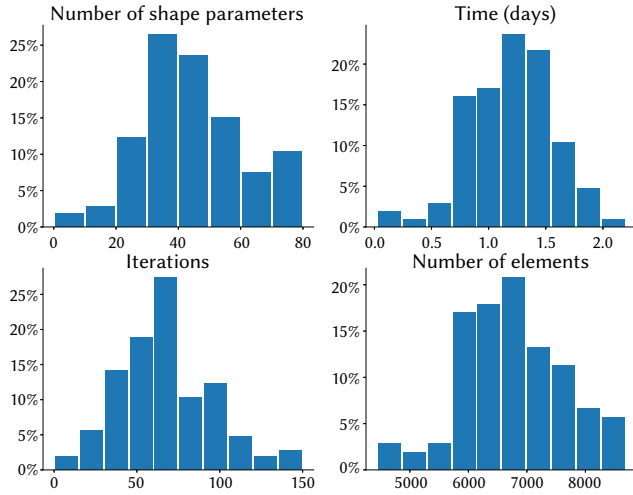
Fig. 11. Statistics of optimizations: Number of shape parameters (top left), total time of the optimizations for each pattern and each target stress (top right), number of iterations for each pattern and each target stress (bottom left), and number of elements in the simulation (bottom right).

corresponding to σ_f does not deviate from σ_f by more than 10%. We show representative examples of shock-protecting lattices, which are fabricated using a Prusa Mk3s printer in TPU (sample size 10cm tall, 2.6cm thick) and physically tested under compression using an INSTRON 5966 Mechanical universal testing machine (Section 4.1). We limit the physical validation to a subset of our microstructure topology due to the time required for each test (~24 hours printing time per sample). We also provide a comparison against the closest known shock-absorbing microstructure (Section 4.5), and conclude the evaluation with ablations (Section 4.8) for the use of a non-linear material model, of a contact model, and for restricting the homogenization to a single axis.

4.1 Microstructure family

To find the material coverage of a microstructure topology, we select 19 homogenized stress targets (from 75 to 75k Pa) and run our incremental optimization to find parameters for a flat response curve for 11 different compressive deformations (from 25% to 75%). We simulate on a base material with Young's modulus 10^6 Pa and Poisson's ratio 0.3, but the behavior of our optimized microstructures is not affected much by the choice of base material (Figure 30). We ran this procedure for 106 topologies, which took 1 week with 200 CPUs (on average 25 min for each optimization) and a maximum memory of 30GB (Figure 11). Then we filtered the curve to find a subset of 5 providing a good coverage (Figure 12). We show the initial guesses, periodic deformations, and physical validations of our optimized microstructures in Appendix E. Once the coverage is obtained, one can adapt to different material models or other variants easily by running optimizations with our optimized structures as initial guesses.

Compression tests. We validate our microstructure family by creating a rectangular object tiled with a grid of cells and performing
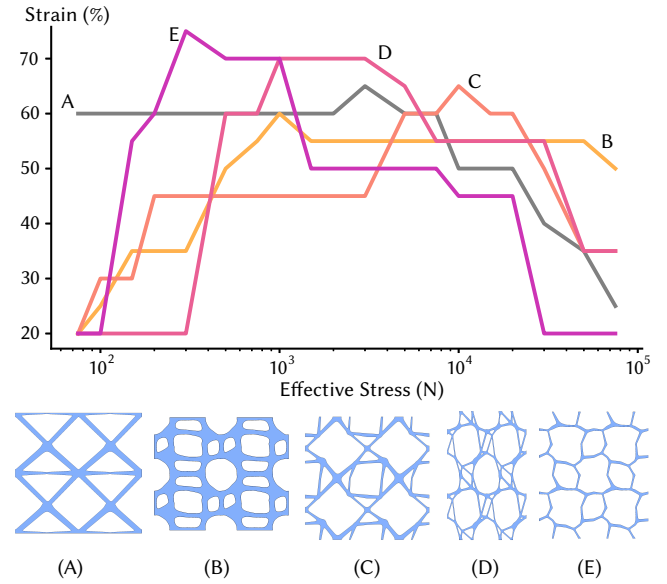
Fig. 12. For each target stress value, we plot the maximal possible strain for which the structures' homogenized stress equals the target. The 5 shown topologies (and their coverage) are selected from a total of 106 topologies to maximize their coverage while providing a compact representation.

a compression test. We perform the compression test virtually (creating a single triangular mesh of the entire object, and simulating it using PolyFEM, using a Neo-Hookean material model, backward Euler time integration, and with contact) and physically, using a universal testing machine. The grid size is the largest possible satisfying the minimal wall thickness of our 3D printer, which is 15 cm. We show the optimized structures and their compression experiments in Figure 37. Figure 1 shows a representative example of three families in our coverage: the virtual compression tests show a good agreement with our homogenized target, and the physical experiments confirm that our physical models are correctly modeling the real-world deformation of an isotropic base material (we used thermoplastic polyurethane for this experiment).

We note that the flat region of force-displacement curves in the compression tests is not as wide as in the periodic homogenization, because in most examples the top and bottom rows are restricted by the planks, so not able to deform as the periodic cells. The flat region can be widened by stacking more rows, but our fabrication is limited by the wall size of our 3D printer.

Although the simulation results match the experimental results, the force curves are not a perfect match. The thin beams in most of the microstructures consist of 1 to 2 layers of material, and the printing accuracy is the likely cause of the mismatch.

The geometric variations within a single family are subtle (Figure 13), but lead to very different response curves. Physical validation results are in line with our computational predictions, with a close match on the response curve, despite pushing the resolution of our 3D printer to the limit (many features in our printed sample use only one or two lines of plastic due to resolution limitations of FDM printing).
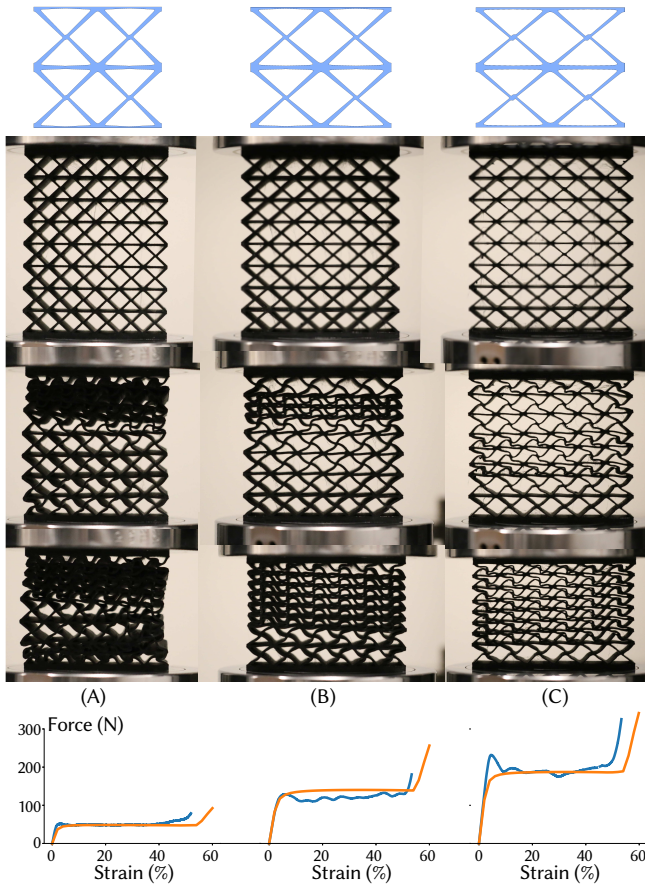
Fig. 13. The unit cell proposed in [Joodaky 2020], parametrized by our shape parameters and then optimized for different effective stresses. We show the rest shapes, compressed shapes, and the force - strain curves of experimental data (blue) and periodic simulation scaled by the dimension of the printed model (orange).

4.2 Stability

The ideal microstructure with a flat stress response may be compressed to different strains under the same amount of force (Figure 37) since the cells are designed to exhibit the same amount of homogenized stress for a wide range of strains. However, this does not affect the overall force of the microstructure or the effectiveness of shock protection, since the rows exhibit the same amounts of force as long as the strains are on the plateau of the stress-strain curve (which starts as small as 5% for most of our optimized structures).

To study the reason why different rows collapse at different speeds, we simulate the compression of a unit-size block with square finite elements and a hypothetical constitutive model that exhibits linearly increasing stress at small strains and almost constant stress (with small oscillations) at larger strains (Figure 15). The compression force in the simulation matches with the analytic stress at small strains (<10%) when the stress is monotonically increasing, and matches closely overall but does not capture the exact oscillations in the analytic stress. In fact, although different rows are
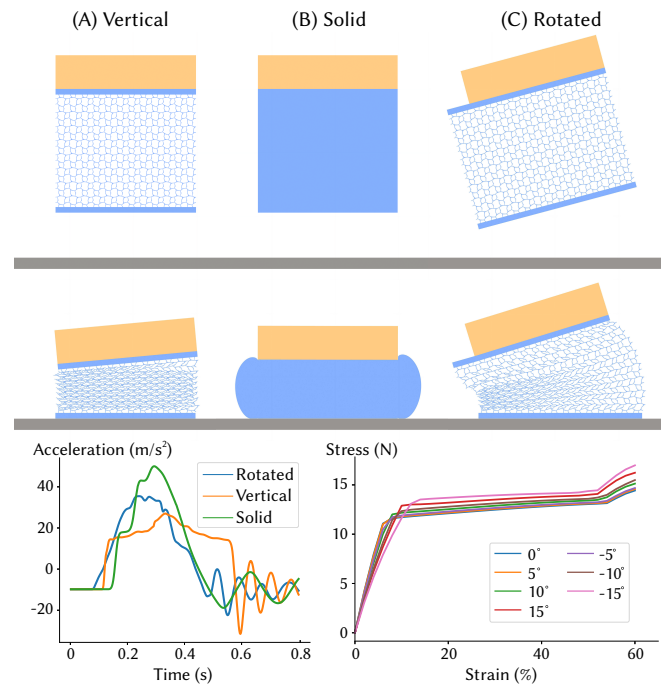
Fig. 14. Drop tests with protecting materials stitched to the bottom of the object. **(A)** Drop vertically with the optimized microstructure attached. **(B)** Drop with a solid material of the same dimension as (A), with smaller Young's modulus so that it compresses by the same distance. **(C)** Drop at an angle with the same load and microstructure, with more columns on the left to reduce tilting. In the acceleration - time plot (bottom left), the maximal acceleration of (A) is around half of (B); the stress-strain curves of this optimized pattern under loads in different angles in homogenizations are shown (bottom right).

at different strains, their compression forces have to be almost the same, as explained in Appendix C, so the overall force does not exhibit the oscillations but is closer to a constant response. In our case, although the periodic stress-strain curves do not have periodic oscillations, other errors in microstructure geometry and fabrication may have a similar influence.

This does not mean that either the periodic or transient full simulations are unstable. Suppose stress-driven homogenization is used, then the compression at different strains with the same homogenized stress are all solutions to the simulation, leading to singular systems in the forward simulation where Newton's method may fail to converge quadratically and the adjoint method may fail to compute the shape derivatives (the assumption that the Hessian is invertible no longer holds). For this reason, we perform strain-driven homogenization (Equation 3) instead, so that the only solution is the deformation at the fixed strain. In this case, in the forward simulation, the Hessian at the minima is positive definite and not ill-conditioned: As shown in Figure 16, the condition number at the deformed state does not increase significantly in the course of the shape optimization, showing that the simulation of the periodic cell with an ideal response remains stable. The condition number at 10% ~25% strain is not significantly larger than at 0% strain (rest shape),
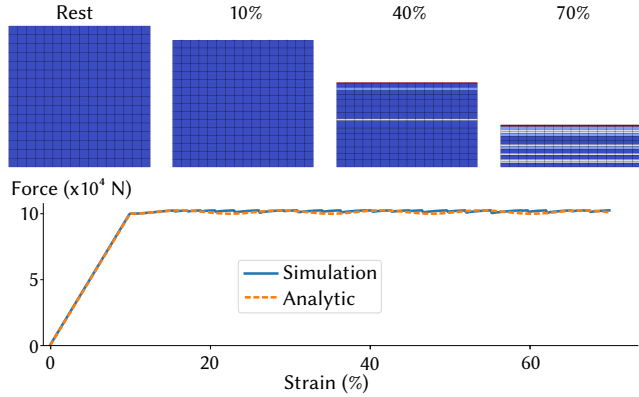
Fig. 15. Compression simulation with a hypothetical constitutive model. Top: Simulation results of compressing a unit-size block, the color shows jacobian of deformed square cells. Bottom: Force-strain plot of the analytic stress (orange) and simulation data (blue).
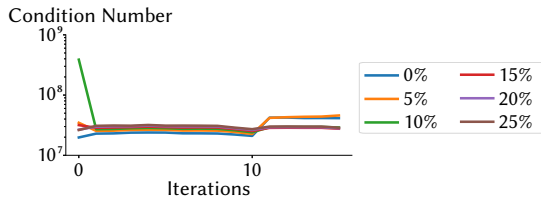

Fig. 16. Plot of the condition number of the Hessian matrix during the shape optimization of the topology (E) in Figure 12. Each curve shows how the condition number at a fixed strain changes in the course of the shape optimization.

showing that the deformation at the flat response region is not ill-conditioned. As a consequence, the Newton's method converges quadratically and the adjoint method works. The reason why transient simulations are stable is more obvious – the inertia guarantees that the energy is locally strictly convex as long as the time step is reasonably small.

Further, in the strain-driven homogenizations, even if the stress-strain curve goes below zero, i.e. the microstructure is bistable around that point, the energy is still strictly convex around the minima and Newton's method can converge as expected, allowing us to optimize for bistability of microstructures (Figure 31).

4.3 Drop tests

Baseline Comparison. To evaluate the use of our approach to design protective gears or packaging protection, we run simulated drop test experiments, where the microstructure is attached to the falling object (Figure 14). We observe that the flat response of our structure leads to slower deceleration of the load. In contrast to shock protectors relying on plastic material [Acanfora et al. 2022], our structure returns to its rest state after impact, making it reusable.

Rotated Load. To evaluate the effectiveness of the optimized structures under shocks in perturbed directions, we pick one topology, perturb the load direction by 15°, and optimize the stress-strain
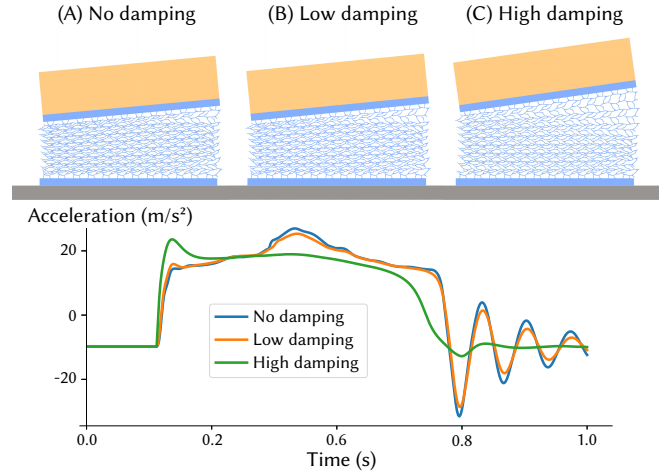
Fig. 17. Drop tests with damping and same setup as in Figure 14 (A). **(A)** $\psi = \phi = 0$, **(B)** $\psi = \phi = 0.5$, **(C)** $\psi = \phi = 5$

curves to be constant in both the vertical direction and the perturbed direction. We then simulate the drop test (Figure 14) with a vertical load and a load rotated by 15°, with the same density (Figure 14). The experiment shows that our structures can be optimized for multiple load directions: The stress-strain plot shows that the rotated drop has only a slightly higher acceleration than the vertical one.

Visco-elasticity. To analyze the influence due to visco-elasticity, we add the strain-rate proportional damping from [Brown et al. 2018] into our transient simulations. We observe that its effect is negligible: the maximal acceleration with and without damping is similar (Figure 17). The oscillations of the curves are reduced as expected, which is a positive side effect but not our goal. We thus opted not to include the dynamics effects, and as a consequence, visco-elasticity in the optimization, as it has a negligible effect on maximal acceleration and a high computational cost [Huang et al. 2024].

4.4 Package protection

A natural application of our microstructures is package protection. We pick the optimized shape in Figure 14, which can protect from shocks in multiple directions. We then generate a quadrilateral mesh covering the object and map the unit cell to every quadrilateral to form a protective shell (Figures 1 and 18). As shown in Figure 19, from the initial geometry to the optimized microstructure, the maximum stress on the object is reduced from 1.2×10^5 Pa to 3.4×10^4 Pa. To make a fair comparison, the density of the microstructure is much lower than the duck so that the total load is not affected by the microstructure infill volume ratio.

4.5 Baseline comparisons

We compare with the state-of-the-art structure proposed in [Joodaky 2020]. This extended χ-shaped structure has been discovered by
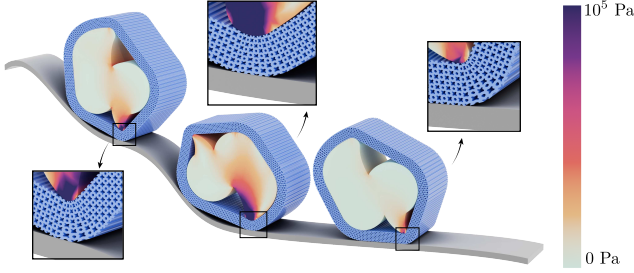
Fig. 18. A duck falls down the slope with un-optimized microstructures as protecting material. The Von Mises stress distribution is shown, same color scale applies to Figure 1.
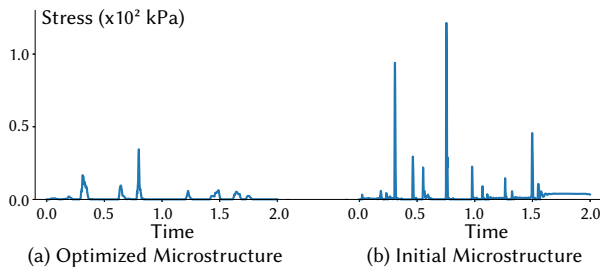

Fig. 19. Max Von Mises stress plots of Figures 1 and 18. The maximum stress is reduced by 72% by optimizing the protecting microstructures.

manual design of its topology. In Figure 20, we show that our optimization approach can modify its effective stress value by optimizing geometric parameters and obtaining a wider range of strain with a constant effective stress value. Additionally, our extensive search of 105 topologies led to connectivities that can achieve higher compression with a flat response, extending the 55% of the baseline up to 70% (Figure 20 and 12).

4.6 Comparison with transient shape optimizations

Figure 13 in [Huang et al. 2024] runs shape optimization on the transient drop test simulation directly by minimizing the L^4 norm of stress on the load on top. To make a fair comparison, we pick the same topology and same shape parametrization (i.e. exactly the same shape design space), and optimize in the homogenization to obtain the ideal shock-protecting structure with desired effective stress. In Figure 21, our optimized structure has a much wider flat range (55%) in the stress-strain plot, so the effective stress can be smaller while absorbing the same amount of energy. We then run exactly the same transient drop simulation with our method, and it shows that our method further reduces the L^4-norm of stress on the load and the maximum de-acceleration of the load, while providing 47% more total impulse during the shock. This shows that homogenization helps obtaining an even better result (with much less time and memory as in Table 1) than optimizing a complete structure consisting of many cells directly.
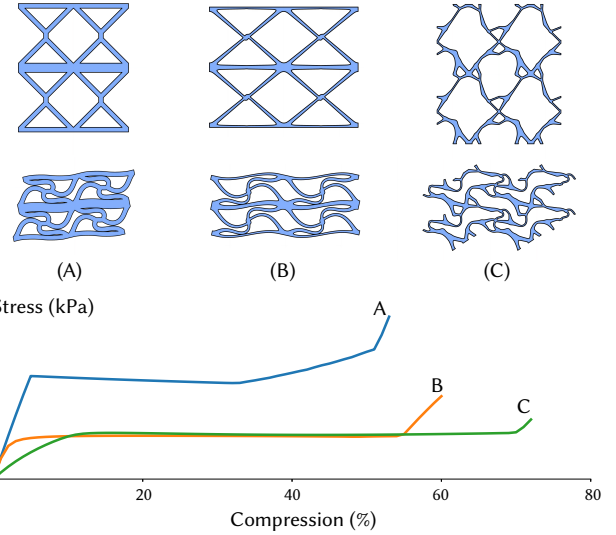

Fig. 20. The flat response of the topology and geometry proposed in [Joodaky 2020] (A), can be considerably extended by optimizing its geometric parameters using our approach (B). Our microstructure family has a different connectivity (C), which provides an even wider flat response. We show on the top the geometry of the corresponding cells in rest pose (top row) and compressed at 50% (bottom row).

Table 1. **Comparison with [Huang et al. 2024].** We report the statistics of the shape optimization in Figure 21. Columns from left to right: peak memory (Gb), number of iterations in the shape optimization, total time of the optimization (min), and average time of each simulation (min).

	Memory	Iterations	Total time	Simulation avg.
[Huang et al. 2024]	9.9	9	561	18
Ours	5.2	33	239	4

4.7 Drop experiment

To further validate the shock-protecting effect of our microstructure family, we perform a drop experiment on one of our optimized microstructures (Figure 22). We fabricate the microstructure in Figure 13 of size $7 \times 7 \times 7$ cm with resin (RESIONE F80 printed on a Phrozen 8k Mighty printer) and drop a glass Christmas ball filled with 200 g of small metal balls onto it. The microstructure protects the ball, reaching 50% compression at the peak, preventing it from breaking. With a solid cube at the bottom, the ball shatters when it hits the ground.

4.8 Ablation study

We provide a series of ablation experiments to motivate our choice of shape representation, including contact forces in homogenization, using a non-linear material model, and using 2×2 tile in homogenizations.

Shape representation. Topology optimization is widely used in shape design for microstructures [Li et al. 2022; Wallin and Tortorelli 2020b; Zhang and Khandelwal 2019]. To compare to our choice of shape representation (Figure 4) in the optimization, we perform
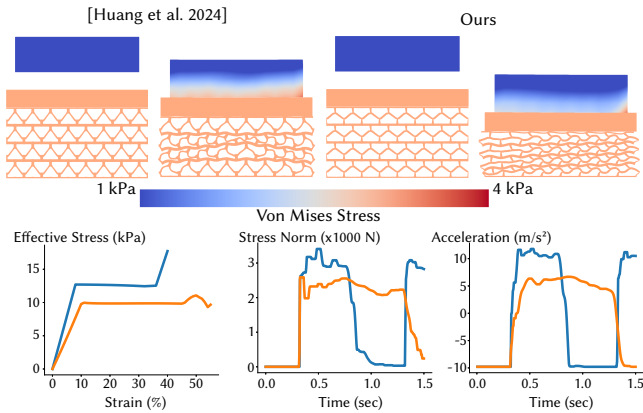
Fig. 21. Top: Rest configuration and largest compression frame of [Huang et al. 2024] and our optimized shape (with Von Mises stress distribution shown). Bottom: Stress-strain curves (left) in homogenization, L^4 norm of stress (middle) and acceleration (right) over time in the transient drop simulation. The optimized microstructure in [Huang et al. 2024] (blue) is flat up to 35%, while ours (orange) has an almost flat response up to 55%, resulting in lower de-acceleration and stress in the drop simulation. The total impulse of our microstructure during the first shock, i.e. area below the first bump of the curve in the right plot, is 47% more than [Huang et al. 2024].

Fig. 22. Drop experiment with a glass Christmas ball with infill. The pictures before (left) and after the shock with a solid cube (middle) and optimized microstructure (right) at the bottom are shown.

the nonlinear homogenization on the optimized extended χ-shaped structure using topology optimization. We rasterize the shape and assign Young's modulus $E = 10^6$ Pa to solid cells and $E = 10^{-2}$ Pa to void cells. In Figure 23, the shape of void cells is close to singular when solid cells approach contact, resulting in convergence issues and poor accuracy in homogenization.

Although there are recent works [Bluhm et al. 2021] able to resolve contact in topology optimization in some cases, robust and accurate handling of contact with topology optimization is largely an open problem as contact behavior can be significantly altered e.g. by artifacts of surface extraction.

Contact. We optimized a pattern without contact forces and compared the stress-strain plots with and without contact forces (Figure 24). While the optimization succeeds, the contact-aware homogenized stress is much higher than expected. Ignoring contact during optimization leads to considerably worse performance, as taking
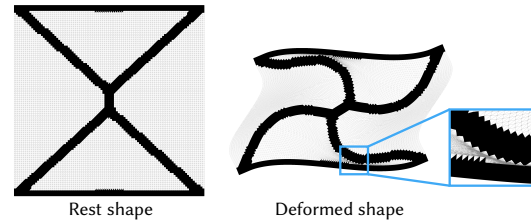

Fig. 23. Homogenization simulated with topology optimization representation. Void cells between beams in contact are highly distorted.
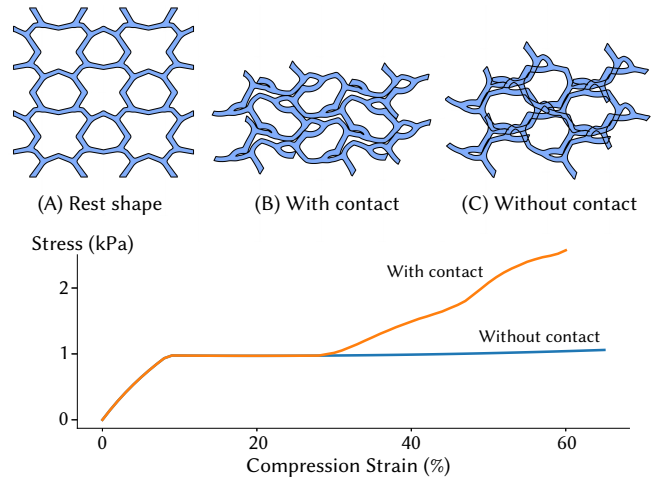

Fig. 24. The microstructure pattern (A) is optimized without contact, we then simulate the shape with (B) and without (C) contact and plot the stress-strain curves.

contact into account is essential for correctly handling large deformations. The contact forces unavoidably introduced in the test lead to a non-flat response for the material optimized without contact, while they are flat for the specimen optimized with contact.

Shear and expansion. To study how much shear and expansion affect the shock-protecting performance, we run the optimization on a couple of examples without shear and expansion penalty. Figure 25 shows the homogenization of an optimized pattern with shear under compression. We then simulate the compression of the full microstructure and experiment on the fabricated result (Figure 26). It is undesirable in common applications where the protecting material is packed into a fixed volume, so we favor patterns that nearly have no shear under compression. For the same reason, we penalize expansion in the horizontal direction as the microstructure is compressed.

Microstructures with negative Poisson's ratio, which shrink in the horizontal direction as they are compressed as in Figure 9, can still fit into a fixed volume. However, the top and bottom planks force the adjacent cells to not shrink, resulting in an hourglass-like shape (in which the top and bottom are wide, while the middle is thin). In this case, the shock-protecting efficiency decreases, and the compression force on the full microstructure increases much faster than the
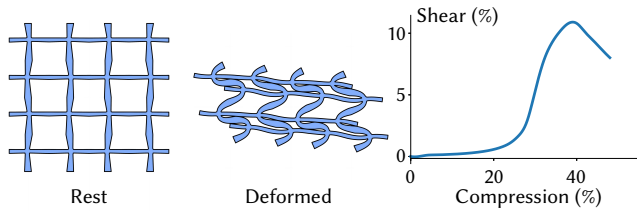
Fig. 25. Optimized pattern with shear under compression. The rest shape and deformation at 50% compression are shown on the left; the shear - compression curve is shown on the right.
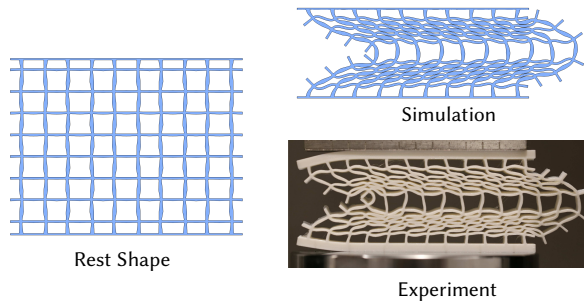

Fig. 26. Full simulation and physical experiment on the optimized pattern in Figure 25. The experiment result matches closely with the simulation.
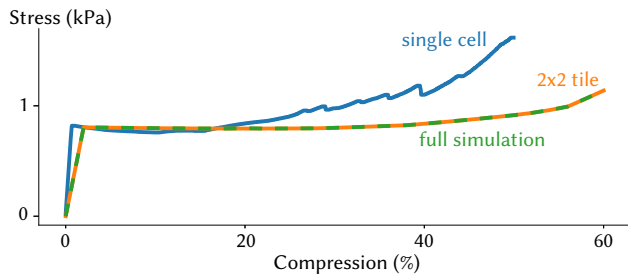

Fig. 27. Stress - compression plot for Figure 9. Homogenization on a single cell (green), homogenization on a 2×2 tile (orange), and full simulation without periodicity (blue). The stress of periodic simulations is scaled to match the dimension of the full simulation.

homogenization stress under compression (Figure 27). Although one way to get around this is to remove the planks and let the top and bottom rows slide freely (by reducing friction coefficients), it's hard in practice to make the surface smooth enough, so we choose to optimize for zero Poisson's ratio.

Symmetry. Symmetric tiles can buckle toward at least two configurations which are energetically equivalent: small imperfections in fabrication or in the load direction will randomly select one. This has a negative effect on large tilings, potentially affecting the overall compression behaviour (Figure 28). Non-symmetric structures are less prone to this issue and we thus do not use symmetric constraints in our microstructure geometry.
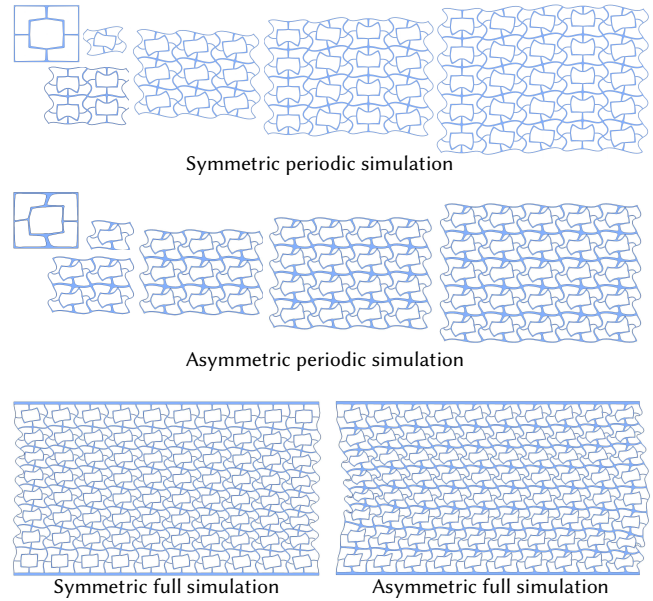

Fig. 28. Periodic and full simulations on symmetric and asymmetric cells. The periodic deformation of asymmetric cells is consistent between small and large tiles (bottom), and matches with the full simulation; while for symmetric cells the deformation on large tiles may consist of different deformation patterns (top), which is inconsistent with the full simulation.

Material model. We advocate for using a non-linear constitutive law for the base material to more accurately capture large deformations. In Figure 29 we reproduce the physical testing of one of our samples with the linear elastic model and the nonlinear Neo-Hookean model, using the same material parameters. The linear model diverges from the nonlinear model at large strains (> 5%) while the nonlinear model matches closely to the physical testing, confirming that a non-linear material model is essential for shock-protecting materials. We performed the same physical testing 10 times, and recorded the first and last curves in Figure 29, to show that the microstructure is capable of protecting against periodic shocks.

Base material. Our optimized patterns are not sensitive to the choice of base material. In Figure 30, we run full-scale compression simulations on the microstructure tiling (C) in Figure 13 with different base materials. The curves are nearly overlapping for a wide range of material choices.

4.9 Bistable shock-protecting structure

Our method can also optimize microstructures with a non-flat stress-strain curve. To demonstrate this we set up an experiment to reproduce the bi-stable microstructure introduced in [Shan et al. 2015]. We reproduce the topology of their microstructure in our shape representation, but not the geometry. The initial shape (Figure 31, C) is not bistable and we optimize the stress-strain curve so that it interpolates some prescribed points to become bistable (Figure 31, D). To confirm the bi-stable behavior, we fabricate the optimized
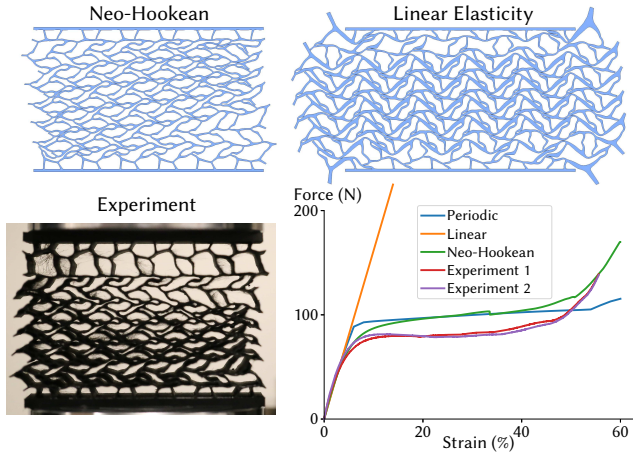
Fig. 29. Compression and corresponding force - strain curves of the optimized microstructure in simulations and experiments. The "Periodic" curve in the plot is scaled by the dimension of the 3D model.
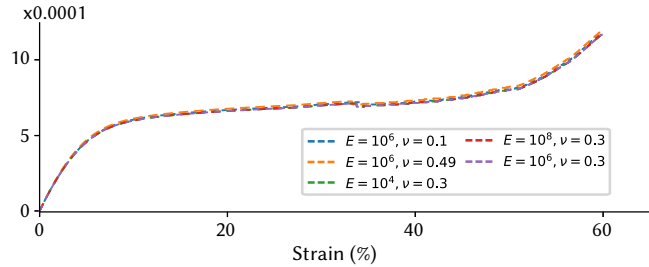

Fig. 30. Full-scale simulations on the microstructure tiling (C) in Figure 13 with different base materials. The Y axis is the ratio between the compression force and Young's modulus.

bistable microstructure and measured the stress-strain curve (Figure 31). The compressed microstructure stays compressed after the compressive force is removed. In our experiment, only the middle layer stays compressed due to the boundary effect on the left and right sides (as shown in the video).

5 CONCLUSIONS

We presented a method for shape optimization of homogenized microstructure materials accounting for large deformation and contact. We used our approach to discover the first family of shock-absorbing microstructures a close to flat strain-stress curve up to 75% compression with varying effective stresses. Finally, we validated it both in simulation and physical experiments.

Our work opens the door to optimizing metamaterial families with non-linear materials and contact forces, and there are many exciting directions for future works: (1) extension to shapes with complex geometrical boundaries, for example using rhombic cells [Tozoni et al. 2021], (2) add a plasticity model, and (3) extend the construction to 3D microstructures.

There are a couple of limitations to our method. First, since the homogenization problem is nonconvex and highly nonlinear, the

(A) Periodic Plot

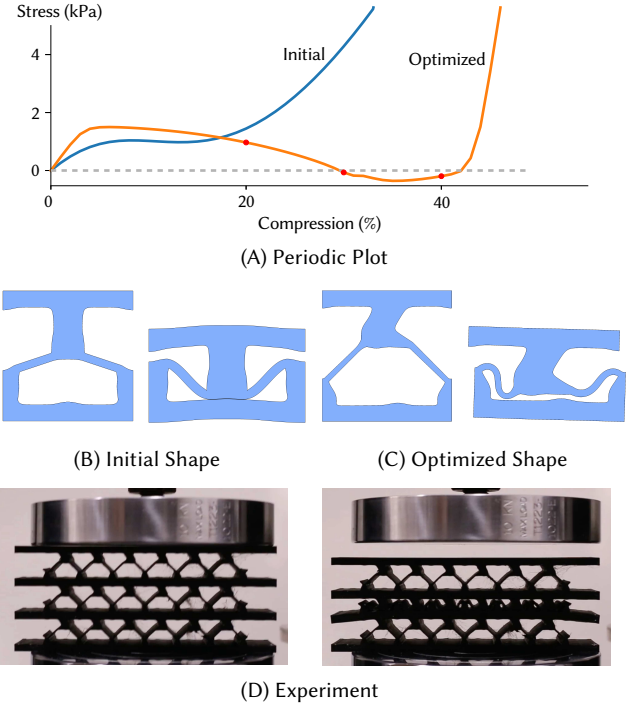(B) Initial Shape   (C) Optimized Shape

(D) Experiment

Fig. 31. Optimized bistable microstructure. (A) The initial blue curve is optimized to the orange curve to interpolate the red points, with negative stress from 30% to 40% strain. (D) The compressed microstructure stays stable after the compression force is released.

solution to the forward problem may jump from one local minima to another under small shape perturbation, so the objective can sometimes be non-deterministic and discontinuous and cause line search failure. Second, the internal deformation of microstructures may be large, requiring the base material to have high elongation at break and elasticity.

To foster reproducibility and adoption of this technique, we will release both our microstructure family and a reference implementation of our optimization pipeline.

REFERENCES

Valerio Acanfora, Rossana Castaldo, and Aniello Riccio. 2022. On the effects of core microstructure on energy absorbing capabilities of sandwich panels intended for additive manufacturing. *Materials* 15, 4 (2022), 1291.

Christie Alappat, Achim Basermann, Alan R. Bishop, Holger Fehske, Georg Hager, Olaf Schenk, Jonas Thies, and Gerhard Wellein. 2020. A Recursive Algebraic Coloring Technique for Hardware-Efficient Symmetric Sparse Matrix-Vector Multiplication. *ACM Trans. Parallel Comput.* 7, 3, Article 19 (June 2020), 37 pages.

Grégoire Allaire. 2002. *Shape Optimization by the Homogenization Method.* Number v. 146 in Applied Mathematical Sciences. Springer. http://books.google.com/books?id=iJCnAlSMVskC

Reza Behrou, Maroun Abi Ghanem, Brianna C Macnider, Vimarsh Verma, Ryan Alvey, Jinho Hong, Ashley F Emery, Hyunsun Alicia Kim, and Nicholas Boechler. 2021. Topology optimization of nonlinear periodically microstructured materials for tailored homogenized constitutive properties. *Composite Structures* 266 (2021), 113729.

Martin Philip Bendsøe. 1989. Optimal shape design as a material distribution problem. *Structural optimization* 1, 4 (1989), 193–202.

Martin Philip Bendsøe and Ole Sigmund. 2003. *Topology optimization: theory, methods and applications.* Springer.

Katia Bertoldi, Pedro M. Reis, Stephen Willshaw, and Tom Mullin. 2010. Negative Poisson's Ratio Behavior Induced by an Elastic Instability. *Advanced Materials* 22, 3 (2010), 361–366. https://doi.org/10.1002/adma.200901956 arXiv:https://onlinelibrary.wiley.com/doi/pdf/10.1002/adma.200901956

Gore Lukas Bluhm, Ole Sigmund, and Konstantinos Poulios. 2021. Internal contact modeling for finite strain topology optimization. *Computational Mechanics* 67, 4 (2021), 1099–1114. https://doi.org/10.1007/s00466-021-01974-x

Matthias Bollhöfer, Aryan Eftekhari, Simon Scheidegger, and Olaf Schenk. 2019. Large-scale Sparse Inverse Covariance Matrix Estimation. *SIAM Journal on Scientific Computing* 41, 1 (2019), A380–A401.

Matthias Bollhöfer, Olaf Schenk, Radim Janalik, Steve Hamm, and Kiran Gullapalli. 2020. State-of-the-Art Sparse Direct Solvers. (2020), 3–33.

George E. Brown, Matthew Overby, Zahra Forootaninia, and Rahul Narain. 2018. Accurate Dissipative Forces in Optimization Integrators. *ACM Trans. Graph.* 37, 6, Article 282 (dec 2018), 14 pages. https://doi.org/10.1145/3272127.3275011

Jonathan Bunyan and Sameh Tawfick. 2019. Exploiting structural instability to design architected materials having essentially nonlinear stiffness. *Advanced Engineering Materials* 21, 2 (2019), 1800791.

Yunteng Cao, Masoud Derakhshani, Yuhui Fang, Guoliang Huang, and Changyong Cao. 2021. Bistable structures for advanced functional systems. *Advanced Functional Materials* 31, 45 (2021), 2106231.

Tian Chen, Julian Panetta, Max Schnaubelt, and Mark Pauly. 2021. Bistable auxetic surface structures. *ACM Transactions on Graphics (TOG)* 40, 4 (2021), 1–9.

Xueyan Chen, Qingxiang Ji, Jianzheng Wei, Huifeng Tan, Jianxin Yu, Pengfei Zhang, Vincent Laude, and Muamer Kadic. 2020. Light-weight shell-lattice metamaterials for mechanical shock absorption. *International Journal of Mechanical Sciences* 169 (2020), 105288.

Yanyu Chen, Tiantian Li, Zian Jia, Fabrizio Scarpa, Chun-Wei Yao, and Lifeng Wang. 2018. 3D printed hierarchical honeycombs with shape integrity under large compressive deformations. *Materials & Design* 137 (2018), 226–234.

G DeBotton, I Hariton, and EA Socolsky. 2006. Neo-Hookean fiber-reinforced composites in finite elasticity. *Journal of the Mechanics and Physics of Solids* 54, 3 (2006), 533–559.

Ryan Fancher, Ian Frankel, Kyle Chin, Maroun Abi Ghanem, Brianna MacNider, Logan S Shannahan, James F Berry, Muge Fermen-Coker, Andrew J Boydston, and Nicholas Boechler. 2023. Dependence of the kinetic energy absorption capacity of bistable mechanical metamaterials on impactor mass and velocity. *arXiv preprint arXiv:2301.09149* (2023).

Tobias Frenzel, Claudio Findeisen, Muamer Kadic, Peter Gumbsch, and Martin Wegener. 2016. Tailored buckling microlattices as reusable light-weight shock absorbers. *Advanced Materials* 28, 28 (2016), 5865–5870.

Felix Fritzen and Oliver Kunc. 2018. Two-stage data-driven homogenization for nonlinear solids using a reduced order model. *European Journal of Mechanics-A/Solids* 69 (2018), 201–220.

Aldair E. Gongora, Kelsey L. Snapp, Richard Pang, Thomas M. Tiano, Kristofer G. Reyes, Emily Whiting, Timothy J. Lawton, Elise F. Morgan, and Keith A. Brown. 2022. Designing lattices for impact protection using transfer learning. *Matter* 5, 9 (2022), 2829–2846. https://doi.org/10.1016/j.matt.2022.06.051

Gaël Guennebaud, Benoît Jacob, et al. 2010. Eigen v3. http://eigen.tuxfamily.org.

Chan Soo Ha, Roderic S Lakes, and Michael E Plesha. 2018. Design, fabrication, and analysis of lattice exhibiting energy absorption via snap-through behavior. *Materials & Design* 141 (2018), 426–437.

Zizhou Huang, Davi Colli Tozoni, Arvi Gjoka, Zachary Ferguson, Teseo Schneider, Daniele Panozzo, and Denis Zorin. 2024. Differentiable solver for time-dependent deformation problems with contact. *ACM Trans. Graph.* (apr 2024). https://doi.org/10.1145/3657648 Just Accepted.

Anna Guell Izard, Ricardo Fabian Alfonso, Geoffrey McKnight, and Lorenzo Valdevit. 2017. Optimal design of a cellular material encompassing negative stiffness elements for unique combinations of stiffness and elastic hysteresis. *Materials & Design* 135 (2017), 37–50.

Seung-Yeol Jeon, Beijun Shen, Nicholas A Traugutt, Zeyu Zhu, Lichen Fang, Christopher M Yakacki, Thao D Nguyen, and Sung Hoon Kang. 2022. Synergistic energy absorption mechanisms of architected liquid crystal elastomers. *Advanced Materials* 34, 14 (2022), 2200272.

Amin Joodaky. 2020. *Mechanics and Design of Polymeric Metamaterial Structures for Shock Absorption Applications.* Ph. D. Dissertation. Purdue University Graduate School.

Muamer Kadic, Graeme W Milton, Martin van Hecke, and Martin Wegener. 2019. 3D metamaterials. *Nature Reviews Physics* 1, 3 (2019), 198–210.

Sotiris Kellas and Karen E Jackson. 2010. Deployable system for crash—load attenuation. *Journal of the American Helicopter Society* 55, 4 (2010), 42001–42001.

Oliver Kunc and Felix Fritzen. 2019. Finite strain homogenization using a reduced basis and efficient sampling. *Mathematical and Computational Applications* 24, 2 (2019), 56.

Oliver Kunc and Felix Fritzen. 2020. Many-scale finite strain computational homogenization via Concentric Interpolation. *Internat. J. Numer. Methods Engrg.* 121, 21 (2020), 4689–4716.

Seubpong Leelavanichkul, Andrej Cherkaev, Daniel O Adams, and Florian Solzbacher. 2010. Energy absorption of a helicoidal bistable structure. *Journal of Mechanics of Materials and Structures* 5, 2 (2010), 305–321.

Minchen Li, Zachary Ferguson, Teseo Schneider, Timothy Langlois, Denis Zorin, Daniele Panozzo, Chenfanfu Jiang, and Danny M. Kaufman. 2020. Incremental Potential Contact: Intersection- and Inversion-free Large Deformation Dynamics. *ACM Trans. Graph. (SIGGRAPH)* 39, 4, Article 49 (2020).

Minchen Li, Zachary Ferguson, Teseo Schneider, Timothy Langlois, Denis Zorin, Daniele Panozzo, Chenfanfu Jiang, and Danny M. Kaufman. 2023b. Convergent Incremental Potential Contact. arXiv:2307.15908 [math.NA]

Weichen Li, Fengwen Wang, Ole Sigmund, and Xiaojia Shelly Zhang. 2022. Digital synthesis of free-form multimaterial structures for realization of arbitrary programmed mechanical responses. *Proceedings of the National Academy of Sciences* 119, 10 (2022), e2120563119. https://doi.org/10.1073/pnas.2120563119 arXiv:https://www.pnas.org/doi/pdf/10.1073/pnas.2120563119

Yue Li, Stelian Coros, and Bernhard Thomaszewski. 2023a. Neural Metamaterial Networks for Nonlinear Material Design. *ACM Trans. Graph.* 42, 6, Article 186 (dec 2023), 13 pages. https://doi.org/10.1145/3618325

Kathryn H Matlack, Anton Bauhofer, Sebastian Krödel, Antonio Palermo, and Chiara Daraio. 2016. Composite 3D-printed metastructures for low-frequency and broadband vibration absorption. *Proceedings of the National Academy of Sciences* 113, 30 (2016), 8386–8390.

Shigeki Matsutani. 2012. *Euler's Elastica and Beyond.* https://doi.org/10.7546/jgsp-17-2010-45-86

Jochen Mueller, Kathryn H Matlack, Kristina Shea, and Chiara Daraio. 2019. Energy absorption properties of periodic and stochastic 3D lattice materials. *Advanced Theory and Simulations* 2, 10 (2019), 1900081.

Praveen Babu Nakshatrala, DA Tortorelli, and KB3069875 Nakshatrala. 2013. Nonlinear structural design using multiscale topology optimization. Part I: Static formulation. *Computer Methods in Applied Mechanics and Engineering* 261 (2013), 167–176.

R.W. Ogden. 1992. Nonlinear Elasticity: Incremental Equations and Bifurcation Phenomena. In *Nonlinear Equations in the Applied Sciences*, W.F. Ames and C. Rogers (Eds.). Mathematics in Science and Engineering, Vol. 185. Elsevier, 437–468. https://doi.org/10.1016/S0076-5392(08)62806-4

Julian Panetta, Abtin Rahimian, and Denis Zorin. 2017. Worst-Case Stress Relief for Microstructures. *ACM Transactions on Graphics* 36, 4 (07 2017), 1–16. https://doi.org/10.1145/3072959.3073649

Julian Panetta, Qingnan Zhou, Luigi Malomo, Nico Pietroni, Paolo Cignoni, and Denis Zorin. 2015a. Elastic textures for additive fabrication. *ACM Transactions on Graphics (TOG)* 34, 4 (2015), 135.

Julian Panetta, Qingnan Zhou, Luigi Malomo, Nico Pietroni, Paolo Cignoni, and Denis Zorin. 2015b. Elastic Textures for Additive Fabrication. *ACM Trans. Graph.* 34, 4, Article 135 (July 2015), 12 pages.

Teseo Schneider, Jérémie Dumas, Xifeng Gao, Denis Zorin, and Daniele Panozzo. 2019. PolyFEM. https://polyfem.github.io/.

Jörg Schröder. 2014. A numerical two-scale homogenization scheme: the FE 2-method. *Plasticity and beyond: microstructures, crystal-plasticity and phase transitions* (2014), 1–64.

Christian Schumacher, Bernd Bickel, Jan Rys, Steve Marschner, Chiara Daraio, and Markus Gross. 2015. Microstructures to control elasticity in 3D printing. *ACM Transactions on Graphics (TOG)* 34, 4 (2015), 136.

Christian Schumacher, Steve Marschner, Markus Gross, and Bernhard Thomaszewski. 2018. Mechanical Characterization of Structured Sheet Materials. *ACM Trans. Graph.* 37, 4, Article 148 (jul 2018), 15 pages. https://doi.org/10.1145/3197517.3201278

Sicong Shan, Sung Kang, Jordan Raney, Pai Wang, Lichen Fang, Francisco Candido, Jennifer Lewis, and Katia Bertoldi. 2015. Multistable Architected Materials for Trapping Elastic Strain Energy. *Advanced materials (Deerfield Beach, Fla.)* 27 (06 2015). https://doi.org/10.1002/adma.201501708

Jonathan Richard Shewchuk. 2005. Triangle: Engineering a 2D quality mesh generator and Delaunay triangulator. In *Applied Computational Geometry Towards Geometric Engineering: FCRC'96 Workshop, WACG'96 Philadelphia, PA, May 27–28, 1996 Selected Papers*. Springer, 203–222.

Georg Sperl, Rahul Narain, and Chris Wojtan. 2020. Homogenized Yarn-Level Cloth. *ACM Trans. Graph.* 39, 4, Article 48 (aug 2020), 16 pages. https://doi.org/10.1145/3386569.3392412

Davi Colli Tozoni, Yunfan Zhou, and Denis Zorin. 2021. Optimizing contact-based assemblies. *ACM Transactions on Graphics (TOG)* 40, 6 (2021), 1–19.

Mathias Wallin and Daniel A Tortorelli. 2020a. Nonlinear homogenization for topology optimization. *Mechanics of Materials* 145 (2020), 103324.

Mathias Wallin and Daniel A. Tortorelli. 2020b. Nonlinear homogenization for topology optimization. *Mechanics of Materials* 145 (2020), 103324. https://doi.org/10.1016/j.mechmat.2020.103324

Fengwen Wang, Ole Sigmund, and Jakob Søndergaard Jensen. 2014. Design of materials with prescribed nonlinear properties. *Journal of the Mechanics and Physics of Solids* 69 (2014), 156–174.

Patrick Wieschollek. 2016. CppOptimizationLibrary. https://github.com/PatWie/CppNumericalSolvers.

Tianju Xue and Sheng Mao. 2022a. Mapped shape optimization method for the rational design of cellular mechanical metamaterials under large deformation. *Internat. J. Numer. Methods Engrg.* 123, 10 (2022), 2357–2380.

Tianju Xue and Sheng Mao. 2022b. Mapped shape optimization method for the rational design of cellular mechanical metamaterials under large deformation. *Internat. J. Numer. Methods Engrg.* 123, 10 (2022), 2357–2380. https://doi.org/10.1002/nme.6941 arXiv:https://onlinelibrary.wiley.com/doi/pdf/10.1002/nme.6941

Julien Yvonnet and Q-C He. 2007. The reduced model multiscale method (R3M) for the non-linear homogenization of hyperelastic media at finite strains. *J. Comput. Phys.* 223, 1 (2007), 341–368.

Guodong Zhang and Kapil Khandelwal. 2019. Computational design of finite strain auxetic metamaterials via topology optimization and nonlinear homogenization. *Computer Methods in Applied Mechanics and Engineering* 356 (2019), 490–527. https://doi.org/10.1016/j.cma.2019.07.027

Zhan Zhang, Christopher Brandt, Jean Jouve, Yue Wang, Tian Chen, Mark Pauly, and Julian Panetta. 2023. Computational Design of Flexible Planar Microstructures. *ACM Trans. Graph.* 42, 6, Article 185 (dec 2023), 16 pages. https://doi.org/10.1145/3618396

Bo Zhu, Mélina Skouras, Desai Chen, and Wojciech Matusik. 2017. Two-Scale Topology Optimization With Microstructures. *ACM Trans. Graph.* 36, 4, Article 120b (07 2017). https://doi.org/10.1145/3072959.3095815

A ADJOINT METHOD

We summarize the adjoint method applied to differentiating J below.

Adjoint Method. At the minima of W, in Equation 2, we have $\partial_{\mathbf{v}} W = 0$. Differentiating both sides of the equation with respect to the shape parameters $\mathbf{q}$ we obtain

$$d_{\mathbf{q}} \partial_{\mathbf{v}} W + \partial_{\mathbf{v}}^2 W d_{\mathbf{q}} \mathbf{v} = 0,$$

i.e.

$$d_{\mathbf{q}} \mathbf{v} = -(\partial_{\mathbf{v}}^2 W)^{-1} \partial_{\mathbf{q}} \partial_{\mathbf{v}} W,$$

where $\partial_{\mathbf{v}}^2 W$ is the Hessian of the total energy in the forward simulation.

The gradient of J with respect to $\mathbf{q}$ then can be written as

$$
\begin{aligned}
d_{\mathbf{q}} J &= \partial_{\mathbf{q}} J + \partial_{\mathbf{v}} J d_{\mathbf{q}} \mathbf{v} \\
&= \partial_{\mathbf{q}} J - \partial_{\mathbf{v}} J \left(\partial_{\mathbf{v}}^2 W \right)^{-1} \partial_{\mathbf{q}} \partial_{\mathbf{v}} W.
\end{aligned}
\tag{9}
$$

Suppose p is the solution of the following linear equation

$$p^T \partial_{\mathbf{v}}^2 W = -\partial_{\mathbf{v}} J,$$

then it directly follows from (9), $d_{\mathbf{q}} J$ can be simplified to

$$d_{\mathbf{q}} J = \partial_{\mathbf{q}} J + p^T \partial_{\mathbf{q}} \partial_{\mathbf{v}} W.$$

Thus, to compute the shape derivative we need to compute $\partial_{\mathbf{v}} J$, $\partial_{\mathbf{q}} J$, $\partial_{\mathbf{q}} \partial_{\mathbf{v}} W$ and solve a linear equation with the same coefficient matrix as the linear system in the forward newton solve.

B ALGORITHM

The main function is OPTIMIZATION($\mathbf{q}_0, \epsilon$), where $\mathbf{q}_0$ are the initial shape parameters, and ϵ is the list of values of vertical strain for which we evaluate the stress-strain curve. After every optimization finishes, we plot the stress-strain curve with dense samples (every 1%) to verify the optimized result: if the homogenized stress at every sample point in the range is within 10% of the target stress, we accept the optimized result; otherwise, we reject it and stop optimizing for larger strain range.

Function *Solve* solves a sequence of problems for increasing deformations G^{11}, using the previous result as initialization, and calling INCREMENTALSOLVE, which imposes a constraint on G^{11} as a penalty with increasing weight, as this leads to a more reliable optimization behavior. NEWTONSOLVE is a standard Newton method, with line search ensuring no self-intersections or element inversion [Li et al. 2020]. It uses the FORCESPD function to ensure that the Hessian approximation used in the solve for the descent direction is always positive-definite. CONSTRAINEDNEWTONSOLVE is similar to NEWTONSOLVE, but with G^{11} fixed to the input scalar strain ϵ.

The algorithm uses a few auxiliary functions for which we do not provide explicit pseudocode as they are either standard or described in other papers:

- INFLATE is the mapping from shape parameters to the discretized domain (Section 6 of [Panetta et al. 2017]);
- LBFGSB returns the descent direction using the L-BFGS solver [Wieschollek 2016] with box constraints;
- LINESEARCH is the standard back-tracking line search.

---

function OPTIMIZATION($\mathbf{q}_0$, ϵ)
    $\mathbf{q} \leftarrow \mathbf{q}_0$
    $I \leftarrow 0$ ▷ Number of iterations
    $\Omega \leftarrow$ INFLATE($\mathbf{q}$) ▷ Section 3.3
    $\tilde{\mathbf{u}}, G \leftarrow$ SOLVE(Ω, ϵ) ▷ Section 3.4
    $J \leftarrow$ OBJECTIVE($\mathbf{q}, \tilde{\mathbf{u}}, G$) ▷ Section 3.5
    $\mathbf{g} \leftarrow \nabla$OBJECTIVE($\mathbf{q}, \tilde{\mathbf{u}}, G$) ▷ Section 3.6
    repeat
        $\mathbf{p} \leftarrow$ LBFGSB($J, \mathbf{g}$) ▷ Descent Direction
        $\alpha \leftarrow$ LINESEARCH($\mathbf{q}, \mathbf{p}$)
        $\mathbf{q} \leftarrow \mathbf{q} + \alpha\mathbf{p}$
        $\Omega \leftarrow$ INFLATE($\mathbf{q}$) ▷ Section 3.3
        $\tilde{\mathbf{u}}, G \leftarrow$ SOLVE(Ω, ϵ) ▷ Section 3.4
        $J \leftarrow$ OBJECTIVE($\mathbf{q}, \tilde{\mathbf{u}}, G$) ▷ Section 3.5
        $\mathbf{g} \leftarrow \nabla$OBJECTIVE($\mathbf{q}, \tilde{\mathbf{u}}, G$) ▷ Section 3.6
        $I \leftarrow I + 1$
    until $\|\mathbf{g}\| < \varepsilon_0$ or $\|J\| < \varepsilon_1$ or $I > IterMax$
    return q
end function

```
function SOLVE(Ω, ε)
    ũ[0] ← 0
    G[0] ← 0
    for k ← 1 to length(ε) do
        ũ[k], G[k] = INCREMENTALSOLVE(ũ[k−1], G[k−1], ε[k])
    end for
    return ũ, G ▷ List of solutions
end function
```

```
function INCREMENTALSOLVE(ũ₀, G₀, ε_Target)
    ũ ← ũ₀
    G ← G₀
    w ← w₀ ▷ Initial weight, initially 10⁴
    e₀ ← |G¹¹ − ε_Target|
    e ← e₀
    repeat
        ũ, G ← NEWTONSOLVE(ε_Target, w, ũ, G)
        e ← |G¹¹ − ε_Target|
        w ← 2w
        if e > e₀ then ▷ Worse than initial solution
            w₀ ← w
            [ũ, G] ← [ũ₀, G₀]
        end if
    until e < ε₂
    G¹¹ ← ε_Target
    ũ, G ← CONSTRAINEDNEWTONSOLVE(ε_Target, ũ, G) ▷ Fix G¹¹ in
the solve
    return ũ, G
end function
```

```
function NEWTONSOLVE(ε, w, ũ, G)
    W̃ ← W(ũ, G) + w|G¹¹ − ε|² ▷ Energy to be minimized
    repeat
        H ← FORCESPD(∇²W̃(ũ, G))
        p ← −H⁻¹∇W̃(ũ, G) ▷ Descent Direction
        α ← CONSTRAINEDLINESEARCH(ũ, G, p)
        [ũ, G] ← [ũ, G] + αp
    until ‖∇W(ũ, G)‖ < ε₁
    return ũ, G
end function
```

```
function FORCESPD(H)
    β ← 10⁻⁸
    H̃ ← H
    while H̃ is not SPD do
        H̃ ← H + βI
        β ← 10β
    end while
    return H̃
end function
```
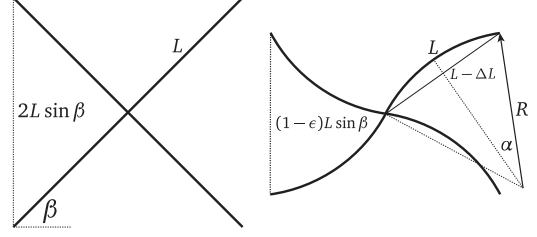

Fig. 32. Geometry of a pure-bending, constant-curvature χ-structure.

C ANALYTIC APPROXIMATION TO THE χ-STRUCTURE.

To elucidate the physical mechanism making the flat stress response possible, we consider a χ-structure, shown in Figure 32, assembled from ideal beams in length-preserving beams in the pure bending state. This is a good approximation of thin beams, as the bending energy for small beam cross-section is lower than the extension/-compression energy. We approximate the deformation of each beam under compression by a constant-curvature deformation, i.e., a circular arc. The structure has a single geometric parameter, the angle β. We also introduce the length of the beams L, but the choice of length does not have an impact on the result. Suppose we impose vertical strain ϵ and zero horizontal strain. With constant-curvature assumption, we can compute the elastic energy W of the deformed state explicitly, from which we can infer the stress-strain dependence, with stress $\sigma = dW/d\epsilon$.

For a beam of constant curvature $\kappa = 1/R$ and length L, the Euler elastica bending energy is, up to a material-dependent constant, L/R^2 (e.g., [Matsutani 2012]), i.e., it is sufficient to estimate R from ϵ and L. From the geometry of the deformation, we obtain:

$$(L − \Delta L)^2 = (1 − \epsilon)^2 L^2 \sin^2 \beta + L^2 \cos^2 \beta$$
$$\Delta L = L − 2R \sin \alpha \qquad (10)$$

where $\alpha = L/(2R) = \frac{L}{2}\kappa$

Up to higher order terms, from the first equation, we obtain $\Delta L = L\epsilon \sin \beta^2$, and from the second equation, $\sin \alpha / alpha = 1 − \Delta L/L = 1 − \epsilon \sin \beta^2$. As $\sin \alpha / \alpha \approx 1 − \alpha^2/6$, we obtain $\alpha \approx \sqrt{6\epsilon} \sin \beta$, and $W(\epsilon) = \kappa^2 L = 4\alpha^2/L \approx 24\epsilon \sin^2 \beta/L$.

From this expression, we conclude that for small deformations, the stress $dW/d\epsilon \approx \sin^2 \beta/L$ does not change with stress. In fact, as Figure 33 shows, even for high ϵ the behavior of α^2 and therefore W is close to linear, so the stress-strain response remains close to flat. The key observation is that by converting compression of the lattice cells into beam bending, instead of the energy depending on the strain quadratically, leading to the common linear stress-strain curve, the energy depends on the strain linearly.

D STRAIN VARIATION UNDER COMPRESSION

A multilayer structure consisting of cells optimized for a flat stress-strain curve can exhibit complex internal behavior depending on small fluctuations of the effective stress-strain without changing the overall response.

Consider a homogeneous block of material of height L compressed in one direction y with (overall) stress-strain response $\sigma = f(\epsilon)$, compressed to a vertical (overall) strain $\epsilon_0 := \frac{1}{L} \int_0^L \epsilon dy$. We consider
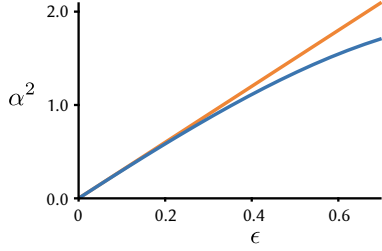
Fig. 33. Precise energy - strain curve, for the pure-bending, constant-curvature χ-structure (blue) is close to linear (red).
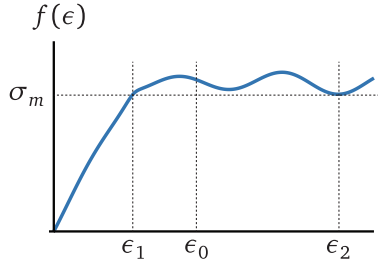

Fig. 34. Notation for analysis of non-monotonic stress-strain curves.
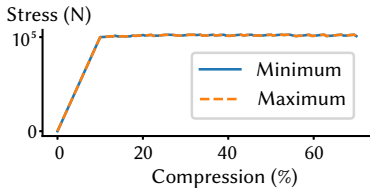

Fig. 35. Maximum and minimum stress over all cells in Figure 15. The relative difference between the maximum and minimum at each strain is within 10^{-6}.

the distributions of strain and stress over the material block below. Assume that the Poisson ratio is zero for simplicity so that both strain and stress are one-dimensional. Assume for force equilibrium over the material block, then from the 1D Cauchy equation, $\partial \sigma / \partial y = 0$, i.e. the stress (denoted as σ_0) is constant over the whole block. If $f(\epsilon)$ is strictly monotonic over ϵ, this also implies constant strain over the block, as for the constant stress σ_0, corresponding constant pointwise strain ϵ_0 is determined uniquely. Figure 36 verifies that when the stress-strain curve is strictly monotonic, the compression of the microstructure is uniform, unlike Figure 13 where rows collapse in random order. For non-strictly monotonic $f(\epsilon)$ the situation may be different: there may be vertical ranges of the block with the same stress but different strains ϵ_i, with equal values of $f(\epsilon_i) = \sigma$. Observe, however, that the total elastic energy is

$$\int_0^L \epsilon f(\epsilon) dy = \sigma_0 \int_0^L \epsilon dy = L\epsilon_0 \sigma,$$

which is deterministic and simply proportional to σ_0, irrespective of the indeterministic distribution of strains.
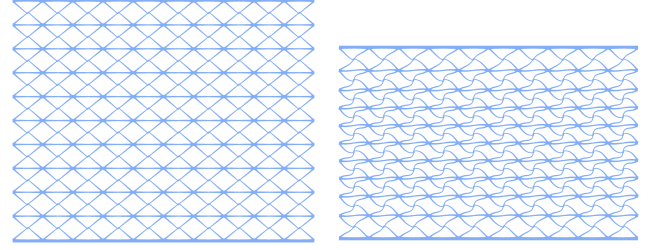
Fig. 36. Compression of the microstructure with strictly monotonic stress-strain curve is uniform, despite the slightly higher stiffness on top and bottom rows due to the fixed beam.

For the target average strain ϵ_0, consider $\sigma_m = \min_{\epsilon \geqslant \epsilon_0} f(\epsilon)$, and let ϵ_2 be the strain for which σ_m is attained (Figure 34). If $f(\epsilon) > f(\epsilon_0)$ for any $\epsilon > \epsilon_0$ (i.e. $\epsilon_2 = \epsilon_0$), then constant-strain state with stress σ has lowest energy: if the strain were non-constant, at some locations, the strain would be $\epsilon > \epsilon_0$, where $\sigma(\epsilon) > \sigma_m$, as the stress is constant, it is above σ_m everywhere, i.e., the energy is higher. If however, $\epsilon_2 > \epsilon_0$ so that $f(\epsilon_2) < f(\epsilon_0)$, and we assume that $f(0) = 0$, by continuity, there is also another $\epsilon_1 < \epsilon_0$, for which $f(\epsilon_1) = \sigma_m$. Pick, e.g., the minimal one with this property. Then by choosing $L_2 = \frac{\epsilon_0 - \epsilon_1}{\epsilon_2 - \epsilon_1}$ and $L_1 = L - L_2$, for any strain distribution the set with strain ϵ_i with measure L_i, we get energy $L\epsilon_0 \sigma_m$, which is the lowest possible. This holds because for any non-uniform strain distribution, we need to have strains above ϵ_0 and this is the lowest possible stress value in this case, and for a uniform distribution the energy is $\epsilon_0 L f(\epsilon_0) > \epsilon_0 L \sigma_m$. Only the measures of two sets matter, not whether these are contiguous or where the two different stress domains are located, i.e., there are many possible states with the same energy, and the chosen one depends on the deformation history. This is a continuum version of bistability. Figure 35 confirms that in the case where the periodic stress-strain curve oscillates, even though the strains of different rows are different in the microstructure, the stresses of different rows are close to the same.

We conclude that for a range of average strains ϵ_0, the material will form two phases, with two different strains.

The discussion above suggests that the static simulation of an ideal shock-protecting material is possibly non-deterministic, however, transient simulations are still deterministic thanks to the inertia.

E PATTERNS

We perform the compression test virtually and physically, using a universal testing machine. We show the optimized structures and their compression experiments in Figure 37.

The optimization cannot always find a geometry with a flat stress-strain curve for a given cell topology, i.e. the objective (7) may not be close to zero when the optimization converges, in which case we give up on this topology. We show a collection of topologies that fail to reach a flat response in Figure 38.

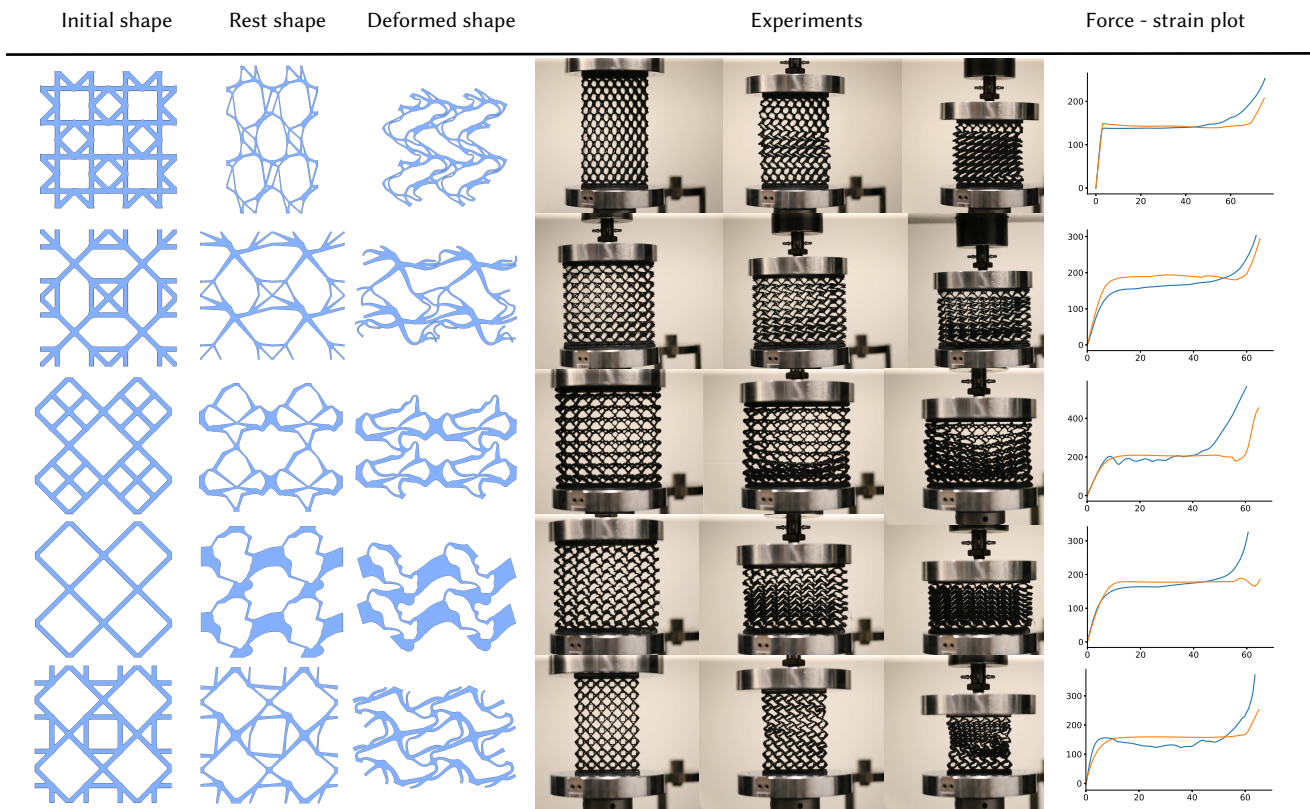| Initial shape	Rest shape	Deformed shape	Experiments	Force - strain plot

Fig. 37. A collection of optimized patterns validated in physical experiments. From left to right: Initial shapes, optimized rest shapes, deformation of optimized shapes, compression experiments, force (N) - strain (%) plots of the experiments (blue), and periodic simulations (orange).
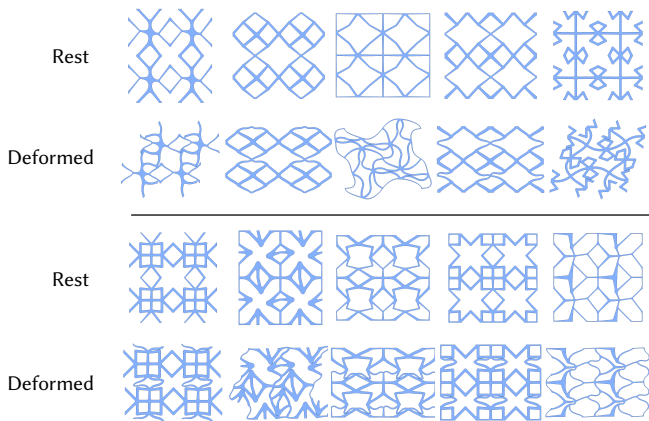

Fig. 38. A collection of topologies that could not be further optimized to fit a constant stress-strain curve up to 25% strain under our constraints.